



RADC-TR-86-174, Vol I (of two) In-House Report October 1986

## ELEMENT PATTERN OF AN AXIAL DIPOLE IN A CYLINDRICAL PHASED ARRAY, PART 1: Theory; PART II: Element Design and Experiments

Boris Tomasic, Alexander Hessel and John C. Herper

APPROVED FOR PUBLIC RELEASE; DISTRIBUTION UNLIMITED



ROME AIR DEVELOPMENT CENTER
Air Force Systems Command
Griffiss Air Force Base, NY 13441-5700

RADC-TR-86-174, Vol I (of two) has been reviewed and is approved for publication.

APPROVED: July William

JOHN K. SCHINDLER

Chief, Antennas & RF Components Branch Electromagnetic Sciences Division

APPROVED: Gelan Collul

ALLAN C. SCHELL

Chief, Electromagnetic Sciences Division

FOR THE COMMANDER:

JOHN A. RITZ

Plans and Programs Division

If your address has changed or if you wish to be removed from the RADC mailing list, or if the addressee is no longer employed by your organization, please notify RADC ( EEA ) Hanscom AFB MA 01731-5000. This will assist us in maintaining a current mailing list.

Do not return copies of this report unless contractual obligations or notices on a specific document requires that it be returned.

#### SECURITY CLASSIFICATION OF THIS PAGE

REPORT DOCUMENTATION PAGE					
18. REPORT SECURITY CLASSIFICATION Unclassified	ne. REPORT SECURITY CLASSIFICATION 1b. RESTRICTIVE MARKINGS Unclassified				
Za. SECURITY CLASSIFICATION AUTHORITY			3. DISTRIBUTION/AVAILABILITY OF REPORT		
26. DECLASSIFICATION/DOWNGRADING SCHED	DULE	Approved for public release; distribution unlimited			
4. PERFORMING ORGANIZATION REPORT NUM	BER(S)	5. MONITORING ORGANIZATION REPORT NUMBER(S)			
RADC-TR-86-174, Vol 1	•				
6. NAME OF PERFORMING ORGANIZATION	8b. OFFICE SYMBOL (If applicable)	7a. NAME OF MONIT	TORING ORGAN	IZATION	
Rome Air Development Center	RADC/EEA	Rome Air De	evelonment	t Center (E	EA)
6c. ADDRESS (City, State and ZIP Code)	JANEO / ELEI	7b. ADDRESS (City,			
Hanscom AFB		Honggom AED			
Massachusetts 01731		Hanscom AFB Massachusetts 01731			
S. NAME OF FUNDING/SPONSORING ORGANIZATION Rome Air	8b. OFFICE SYMBOL (If applicable)	9. PROCUREMENT INSTRUMENT IDENTIFICATION NUMBER			UMBER
Development Center	RADC/EEA				
8c. ADDRESS (City, State and ZIP Code)		10. SOURCE OF FUN	DING NOS.		
Hanscom AFB		PROGRAM ELEMENT NO.	PROJECT NO.	TASK NO.	WORK UNIT
Massachusetts, 01731					
11. TITLE (Include Security Classification)		0110077	2225		
Element Pattern of an Axial I	Dipole (cont.)	61102F	2305	03	03
12. PERSONAL AUTHOR(S) Boris Tomasic, Alexander H					
13a TYPE OF REPORT 13b. TIME C		14. DATE OF REPOR			
In-house FROM 1/80 to 1/85 1986 October 110					
17. COSATI CODES	18. SUBJECT TERMS (C	ontinue on reverse if ne	cessary and identi	ify by block numbe	r)
FIELD GROUP SUR. GR.	Cylindrical a	rrays	•		
09 03		rray antennas			
19. ASST TACT (Continue on reverse if necessary and	Dipole arrays	<u>.</u>			
Cylindrical array antenna			ons requir	ing uniforn	n 360° azi-
muthal pattern performance.					
signs, an accurate knowledge In Part 1 of this report, a	of the mutually	coupled elem	ent pattern	n becomes	important.
periodic array of axial dipole radiators placed coaxially over a circular cylindrical ground. This solution avoids the problems associated with asymptotic approaches and dis-					
plays a number of advantages:					
uniformly valid in all spatial regions for both rectangular and, with a simple modification,					
for triangular isosceles lattice configurations; and (3) It provides absolute gain informa- tion. The analysis is presented along with numerical results for representative parama-					
ter values selected to illustrate the various trade-offs. Comparison with published data					
employing the asymptotic approach and with planar array results is given.					
In Part 2, the design and construction of a cylindrical array of axial dipoles is (cont.)					
20. DISTRIBUTION/AVAILABILITY OF ABSTRACT 21. ABSTRACT SECURITY CLASSIFICATION					
UNCLASSIFIED/UNLIMITED 🖺 SAME AS RPT.	DTIC USERS	Unclassi	fied		
22a. NAME OF RESPONSIBLE INDIVIDUAL		22b. TELEPHONE NI (Include Area Co.		22c. OFFICE SYN	ABOL
Boris Tomasic (617)			-	RADC/I	CEA

EQUALTY CLASSIFICATION OF THIS PAGE

Block 11 (cont.):

in a Cylindrical Phased Array, Part 1: Theory, Part 2: Element Design and Experiments

Block 19 (cont.):

described. Dipole-pattern amplitude measurements performed over practical scan and frequency ranges show excellent agreement with theoretically predicted results. Dipole pattern phase, feed-line effects, and radiator match are also discussed. These results provide strong evidence of the correctness of the analysis and numerical results presented in Part 1 and furnish a firm basis for accurate prediction of array performance.

Unclassified

## Preface

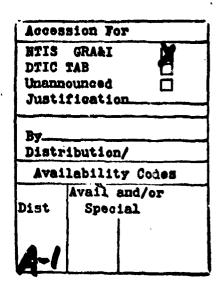
This work was supported by the Sperry Corporation, Great Neck, NY 11020, by the Rome Air Development Center, Electromagnetic Sciences Division, Hansom AFB, MA 01731, and by the Rome Air Development Center, Griffiss AFB, NY 13441.

Boris Tomasic is with the Electromagnetic Sciences Division, Rome Air Development Center, Hanscom AFB, MA 01731.

Alexander Hessel is with the Polytechnic University, Route 110, Farmingdale, NY 11735.

John C. Herper is with the Sperry Corporation, Great Neck, NY 11020.





		Contents
Pa	rt 1	
1.	INTRODUCTION	1
2.	ANALYSIS FOR RECTANGULAR LATTICE	2
	<ul> <li>2.1 Array Model</li> <li>2.2 Active Dipole Current</li> <li>2.3 Active Gap-Impedance</li> <li>2.4 Matching Network and Reflection Coefficient</li> <li>2.5 Active Array Fields</li> <li>2.6 Element Pattern</li> </ul>	2 4 9 9 10 11
3.	Analysis for isosceles triangular lattice	13
	3.1 Array Model 3.2 Active Gap-Impedance and Reflection Coefficient 3.3 Element Pattern	-13 13 15
4.	NUMERICAL ANALYSIS	15
	4.1 Rectangular Lattice 4.2 Triangular Lattice	· 16
5.	NUMERICAL RESULTS AND DISCUSSION	20
	5.1 Rectangular Grid Array 5.2 Triangular Grid 5.3 Comparison With Other Results	21 31 34
6.	CONCLUSION	35
RE	EFERENCES	39
ΑF	PPENDIX A: FLCQUET'S THEOREM FOR ISOSCELES TRIANGULAR ARPAY LATTICE	41

		Potnárie
APPE	NDIX B: SINGLE ELEMENT EXCITATION IN A TRIANGULAR LATTICE	45
APPE	NDIX C: CONVERGENCE ACCELERATION	47
	1. Rectangular Lattice 2. Triangular Lattice	48 49
APPE	NDIX D: MATCHING NETWORKS	51
D	1. Load Impedance Connected to Output Terminals of Two-Port Matching Networks	51
D	2. Load (Dipole Gap Impedance) Connected to Output Terminals of Two-Port Network via Transmission Line	• • • • • • • • • • • • • • • • • • • •
D	3. S-Parameters of the Series Matching Network 4. S-Parameters of a Parallel Matching Network	57 60
D	5. S-Parameters of the Quarter-Wavelength Transformer Matching Network	63
A DDE	NDIX E: ASYMPTOTIC EXPANSIONS OF $Z_{v_m}(\kappa_n *, \kappa_n \rho_0)$	69
	1. Real Arguments	70
	2. Imaginary Arguments	76
APPE	NDIX F: ELEMENT PATTERN PHASE CENTER	81
Part 2		
1. IN	TRODUCTION	83
2. A	RRAY DESCRIPTION	84
3. D	POLE DESIGN	. 86
4. M	EASURED AMPLITUDE PATTERNS	87
5. P	HASE PERFORMANCE	94
6. A	RRAY BEAM FORMING CONSIDERATIONS	94
7. C	ONCLUSION	82
REFE	RENCES	ä
NOMI	ENCLATURE	<b>8</b> £
		Illustrations
Part	1	
1. G	eometry of the Circular Cylindrical Array of Dipoles in a Rectangular Lattice	3

## Illustrations

2.	Unit Cell Geometry of a Cylindrical Dipole Array	4
3.	Equivalent Network for a Dipole Element in a Cylindrical Array	10
4.	Geometry of the Circular Cylindrical Array of Dipoles in a Triangular Lattice	14
5.	Gap-Resistance Rg (0, 0) Versus Number of Dipole Current Terms (b/ $\lambda$ = 0.6, d/ $\lambda$ = 0.7, s/ $\lambda$ = 0.25, w/ $\lambda$ = 0.05, h/ $\lambda$ = 0.01)	18
6.	Gap-Reactance Xg (0, 0) Versus Number of Dipole Current Terms (b/ $\lambda$ = 0.6, d/ $\lambda$ = 0.7, s/ $\lambda$ = 0.25, w/ $\lambda$ = 0.05, h/ $\lambda$ = 0.01)	18
7.	H-Plane Voltage Element Gain Pattern for Cylindrical and Reference Planar Arrays and Matching Networks. (a) Series, (b) Parallel (b/ $\lambda$ = 0.6, d/ $\lambda$ = 0.7, ka = 120)	19
8.	H-Plane Voltage Element Gain Pattern (d/ $\lambda$ = 0.7, ka = 120). Parameter: azimuth spacing b/ $\lambda$ = 0.5, 0.6, 0.7	20
9.	Voltage Element Gain Pattern and Corresponding Local Grating Lobe Diagram (b/ $\lambda$ = 0.6, d/ $\lambda$ = 0.7, ka = 120). Parameter: elevation angle $\theta$ = 30°, 40°,, 90°	23
10.	E-Plane Voltage Element Gain Pattern (b/ $\lambda$ = 0.6, ka = 120). Parameter: axial spacing d/ $\lambda$ = 0.5, 0.6, 0.7	23
11.	H-Plane Voltage Element Gain Pattern (b/ $\lambda$ = 0.6, d/ $\lambda$ = 0.7). Parameter: cylinder radius ka = 30, 60, 240 (for ka = 120, see Figure 9)	25
12.	H-Plane Element Gain Pattern (dB) (b/ $\lambda$ = 0.6, d/ $\lambda$ = 0.7). Parameter: cylinder radius ka = 30, 60, 120, 240	25
13.	Element Gain Pattern (dB) (b/ $\lambda$ = 0.6, d/ $\lambda$ = 0.7, ka = 120). Parameter: elevation angle $\theta$ = 10°, 50°, 90°	26
14.	H-Plane Element Gain Pattern (dB) (d/ $\lambda$ = 0.7, ka = 120). Parameter: azimuth spacing b/ $\lambda$ = 0.5, 0.6, 0.7	26
l 5.	H-Plane Element Phase Pattern (d/ $\lambda$ = 0.7, ka = 120). Parameter: azimuth spacing b/ $\lambda$ = 0.5, 0.6, 0.7	27
l <b>6.</b>	E-Plane Element Phase Pattern (b/ $\lambda$ = 0.6, ka = 120). Parameter: axial spacing d/ $\lambda$ = 0.5, 0.6, 0.7	27
17.	Gap Impedance $Z_g$ (0, 0) Versus Ground Plane Spacing (b/ $\lambda$ = 0.6, d/ $\lambda$ = 0.7, ka = 120, $Z_0$ = 100 $Q$ ). Parameter: dipole length L/ $\lambda$ = 0.4, 0.5, 0.6	29
18.	H-Plane Gap-Impedance Versus Azimuth Scan Angle and E-Plane Gap Impedance Versus Elevation Scan Angle Over $\pm 10$ Percent Frequency Band (b/ $\lambda_c$ = 0.5, d/ $\lambda_c$ = 0.6, ka = 120, $Z_0$ = 100 $Q$ )	29
19.	•	30

## Hlustrations

20.	H-Plane Voltage Element Gain Pattern (b/ $\lambda_c$ = 0.5, d/ $\lambda_c$ = 0.6, ka = 120). Parameter: frequency f = 0.9 f <sub>c</sub> , f <sub>c</sub> , 1.1 f <sub>c</sub>	30
21.	Voltage Element Gain Pattern and Corresponding Local Grating Lobe Diagram [Triangular Grid (a) $b/\lambda = 0.6$ , $d/\lambda = 0.7$ , ka = 120]. Parameter: elevation angle $\theta = 30^{\circ}$ , $40^{\circ}$ ,, $90^{\circ}$	33
22.	Voltage Element Gain Pattern and Corresponding Local Grating Lobe Diagram [Triangular Grid (b) $b/\lambda = 1.2$ , $d/\lambda = 0.35$ , ka = 120]. Parameter: elevation angle $\theta = 30^{\circ}$ , $40^{\circ}$ ,, $90^{\circ}$	33
23.	Comparison of Voltage Element Gain Patterns Between Figure 35 and Results Based on Modal Analysis (b/ $\lambda$ = 0.6, d/ $\lambda$ = 0.54, L/ $\lambda$ = 0.5, s/ $\lambda$ = 0.25, w/ $\lambda$ = 0.05, h/ $\lambda$ = 0.01, ka = 125.7). Parameter: elevation angle $\theta$ = 60°, 90°	36
24.	Comparison of Voltage Element Gain Patterns Between Dipole and Rectangular Aperture Radiators, $\frac{11}{100}$ (b/ $\lambda$ = 0.6, d/ $\lambda$ = 0.8, ka = 105)	36
A1,	Unit Cell Cross Section at $\rho = \rho_0$ of a Circular Cylindrical Array With Triangular Lattice	42
D1.	S-Parameter Representation of a Two-Port Network	52
D2.	Two-Port Matching Network Connecting Load Impedance Z <sub>22</sub> ' With Transmission Line 1	52
D3.	Two-Port Network Connecting Matched-Transmission Line 1 With Transmission Line 2	55
D4.	Load Impedance $Z_g$ Connected to Matching Network via Transmission Line	55
D5.	Series Matching Network	57
<b>b</b> .	Network Illustrating Evaluation of S <sub>11</sub> and S <sub>21</sub> of Series Matching Network	58
D7.	Network Illustrating Evaluation of $S_{22}$ and $S_{12}$ of Series Matching Network	59
D8.	Parallel Matching Network	60
D9.	Network Illustrating Evaluation of S <sub>11</sub> and S <sub>21</sub> of the Parallel Matching Network	62
D10.	Network Illustrating Evaluation of S <sub>22</sub> and S <sub>12</sub> of the Parallel Matching Network	62
D11.	Quarter-Wave Transformer Matching Network	63
D12.	Quarter-Wavelength Transformer Matching Network Illustrating Evaluation of S-Parameters	64
D13.	Network Illustrating Evaluation of S <sub>11</sub> and S <sub>21</sub> of Quarter-Wave Transformer Matching Network	65
D14.	Network Illustrating Evaluation of S22 and S12 of	<b>R</b> R

## Mustrations

## Part 2

1.	Cylindrical Array Test Bed Antenna	84
2.	Column Network With Protective Foam Partially Removed Showing Dipole Radiators	86
3.	Outline Diagram of Folded Dipole Radiator With Stripline Feed	87
4.	Waveguide Simulator for 45° H-Plane, 0° E-Plane Scan.  (a) Simulator body with orthogonal mode transducer.  (b) Test dipole in fixture. (c) Relationship of array lattice to simulator size and location	88
5.	Measured Dipole Impedance in Waveguide Simulator	89
6.	Measured and Theoretical Amplitude Patterns at Center Frequency	90
7.	Amplitude Patterns 4 Percent Above Center Frequency	90
<b>s.</b>	Amplitude Patterns 22.6 Percent Above Center Frequency	91
9.	Amplitude Patterns at Various Elevation Angles. (a) $\hat{\theta} = 0^{\circ}$ , (b) $\hat{\theta} = 10^{\circ}$ , (c) $\hat{\theta} = 20^{\circ}$ , (d) $\hat{\theta} = 30^{\circ}$	92-93
0.	Location of Dipole Phase Center	95
1.	Grating Lobe Level of a Low Sidelobe Pattern Excited by a 120° Cylindrical Array Arc	96

# Element Pattern of an Axial Dipole in a Colondrical Phased Array, Part 1: Theory

#### 1. INTRODUCTION

Circular cylindrical antenna arrays are of interest for radar and communication applications because of the uniformity of their circumferential radiation characteristics. Some cylindrical array applications require a high degree of performance antenna characteristics such as precise beam pointing, accurate angle tracking, ultralow sidelobes, and wide bandwidth. To achieve the associated tight array illumination tolerances, mutual coupling between the radiating elements must be accurately accounted for.

Surveys of the state-of-the-art of cylindrical phased arrays and their design considerations are given. <sup>1,2</sup> However, most of the cited bibliographies deal with aperture arrays. On the other hand, a dipole element is an attractive choice for an array radiator due to its simplicity of manufacture, reasonably wide bandwidth, and polarization purity.

These factors motivated the two-phase effort: theoretical and experimental.

<sup>(</sup>Received for publication 31 January 1984)

Hessel, A. (1972) Mutual coupling effects in circular arrays on cylindrical surfaces - Aperture design implications and analysis, in <u>Phase Array An-</u> tennas, A.A. Oliner and G.H. Knittel, Eds., Artech House, Dedham, Mass.

<sup>2.</sup> Mailloux, R.J. (1982) Phased array theory and technology, <u>Proc. IEEE</u>, 70(No. 3).

In the first phase, cylindrical, stacked, ring-antenna arrays of uniformly spaced axial dipoles were investigated to establish the mutually coupled element pattern characteristics. A detailed account of this investigation is provided in Part 1 of this report and has been briefly reported. The second phase of the study consisted of experiments augmenting and supporting the theoretical phase and is presented in Part 3.

In the theoretical analysis, a modal approach 's employed that utilizes a unit cell method similar to that reported for an array of aperture elements in a circular cylindrical ground. The modal approach was chosen for several reasons. Asymptotic treatments hapes after their numerical validity has been ascertained by comparison with exact solutions of relevant canonical problems. The modal technique avoids the uncertain accuracy of the asymptotic approaches and has the following advantages: (1) In principle, it furnishes an exact solution subject only to truncation errors that can be estimated; (2) It is uniformly valid in all spatial regions, whereas asymptotic formulations employ different representations in various angular domains and require transition functions to connect the results smoothly; (3) It has additional flexibility in that it provides answers for both rectangular and isosceles triangular array lattices, the latter after a minor modification; and (4) It yields both the realized gain and element pattern phase.

#### 2. ANALYSIS FOR RECTANGULAR LATTICE

#### 2.1 Array Model

The cylindrical array model under consideration, shown in Figure 1, consists of an infinite number of equispaced stacked rings of axial dipoles. The rings, of radius  $\rho_0$ , contain N equispaced identical dipoles each located coaxially a distance s above an infinite, perfectly conducting, circular cylindrical surface of radius a.

<sup>3.</sup> Herper, J.C., Hessel, A., Mandarino, C., and Tomasic, B. (1980) Performance of a dipole element in a cylindrical array - A modal approach, IEEE Antennas Propag. Symp. Dig., University of Laval, PQ, Canada, 162-165.

<sup>4.</sup> Sureau, J.C., and Hessel, A. (1971) Element pattern for circular arrays of waveguide-fed axial slits on large conducting cylinders, IEEE Trans. Amennas Propag., AP-19, 64-76.

<sup>5.</sup> Eichmann, G., and Lee, K.S. (1978) Analysis of conformal scanning dipole arrays, Amtennas Propag. Symp. Dig., University of Maryland, Washington, D.C.

<sup>6.</sup> Indenbom, M. V., and Filippov, V.S. (1978) An asymptotic solution of the problem of mutual coupling between the radiators of a convex cylindrical array antenna, Radio Eng. Electron Phys., 23(No. 1), 42-49.

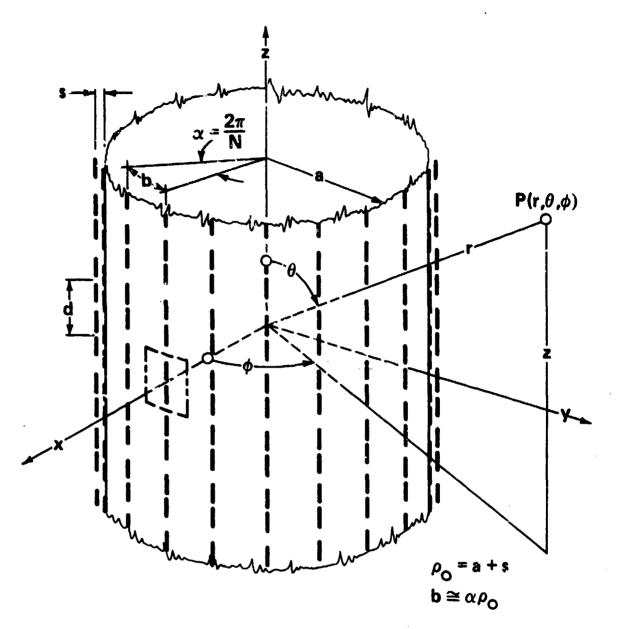


Figure 1. Geometry of the Circular Cylindrical Array of Dipoles in a Rectangular Lattice

The dipoles have a length L, narrow width w, and negligible radial thickness. Their central gaps of length h are excited through identical matching networks via respective transverse electromagnetic (TEM) transmission lines fed from matched generators. For the case of single-element excitation, all but one of the generators are short-circuited. A typical wedge-shaped unit cell, of axial dimension d and width b =  $2\pi\rho_0/\mathrm{N}$  at the dipole location, is seen in Figure 2, which shows a dipole without its feed.

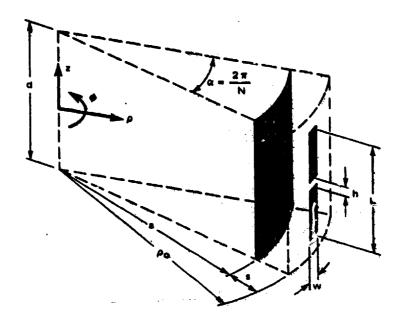


Figure 2. Unit Cell Geometry of a Cylindrical Dipole Array

#### 2.2 Active Dipole Current

The performance of a singly excited dipole in a match-terminated array environment is determined by superposition of fields generated by the various discrete, independent azimuthal phase sequence excitations, as well as by those of the continuous spectrum type, the latter corresponding to uniform-amplitude, progressive-phase axial beam steering. A combination of one of each kind constitutes an active cylindrical array excitation.

As a first step toward analysis of a free-excited array, one considers its forced active excitation. The generic boundary value problem in this case reduces to that of evaluation of fields radiated by a dipole in a radial unit cell with phase-shift walls and excited by a prescribed gap voltage. Such analysis leads to the determination of the unmatched, active dipole gap-impedance as a function of circumferential and axial phasing, frequency, and geometry. With this information, an appropriate matching network may be configured and the element pattern evaluated.

To begin with, one observes that, for  $w/\lambda \ll 1$ , the usual assumption of strictly axial dipole currents should yield a good approximation to the desired dipole performance. As a consequence, all fields may be derived from a single axial component of a vector potential  $A_z$ . The treatment is facilitated by introducing a unit cell Green's function  $G(\underline{r},\underline{r}';\nu,k_{z0})$  which represents, to within a constant factor  $\mu_0$ , the vector potential due to an axial, electric point current element located at  $\underline{r}=\underline{r}'$  in a radial unit cell. Here,  $\nu(\nu=0,1,\ldots,N-1)$  denotes the

circumferential  $\nu$ th phase sequence excitation with a uniform unity amplitude and a phase delay once around the array of  $2\pi\nu$  rad. The argument  $k_{z0}$  indicates that the progressive phase delay between the neighboring elements in any axial column of the active array is  $k_{z0}$ d.

By linearity, the expression for the vector potential in a unit cell due to the dipole surface current density K may be written in the form

$$A_{z}(\underline{r};\nu,k_{zo}) = \mu_{o} \int_{z} G(\underline{r},\underline{r}';\nu,k_{zo}) K(\underline{r}') dS'$$
(1)

where  $\underline{r} = (\rho, \phi, z)$  and S is the dipole surface. Here, G satisfies

$$\nabla^2 \mathbf{G} + \mathbf{k}^2 \mathbf{G} = -\delta(\underline{\mathbf{r}} - \underline{\mathbf{r}}'), \quad \mathbf{k} = \frac{2\pi}{\lambda}$$
 (2a)

and is subject to the following boundary conditions:

$$G(a, \phi, z; \underline{r}^*) = 0 \tag{2b}$$

radiation condition for 
$$\rho \to \infty$$
 (2c)

two Floquet conditions:

$$G(\rho, \frac{\alpha}{2}, z) = e^{-j\nu\alpha} G(\rho, -\frac{\alpha}{2}, z)$$
 (2d)

$$G(\rho,\phi,\frac{d}{2}) = e^{-jk_{zo}d} G(\rho,\phi,-\frac{d}{2}) . \qquad (2e)$$

For  $\mathrm{e}^{\mathrm{j}\omega t}$  time dependence, the various field components are

$$E_z = -\frac{j\omega}{k^2} \left( \frac{\partial^2 A_z}{\partial z^2} + k^2 A_z \right) \tag{3a}$$

$$\mathbf{E}_{\phi} = -\frac{\mathbf{j}\omega}{\mathbf{k}^2 \rho} \frac{\partial^2 \mathbf{A}_z}{\partial \phi \partial z} \tag{3b}$$

$$H_{\phi} = -\frac{1}{\mu_0} \frac{\partial A_z}{\partial \rho} . \tag{3c}$$

From Eqs. (3a), (3b), and (1), it is evident, in view of Eq. (2b), that  $E_z$  and  $E_{\phi}$  vanish at  $\rho$  = a. Also, from Eqs. (1), (2a), and (3c), one finds that

$$H_{\phi}(\rho_0^+, \phi, z) - H_{\phi}(\rho_0^-, \phi, z) = K(z, \phi)$$
 (4)

Finally, to satisfy Eqs. (2d) and (2e), G is expanded in terms of a complete, orthonormal Floquet basis

$$\Phi_{mn}(\phi,z) = \frac{1}{\sqrt{\alpha d}} e^{-j(\nu_m \phi + k_{zn} z)}$$
(5)

where  $\nu_{\rm m} = \nu + {\rm mN}$ ,  $(\nu = 0, 1, ..., N - 1; {\rm m} = 0, \pm 1, ...)$  and  $k_{\rm zn} = k_{\rm z0} + 2\pi {\rm n/d}$ ,  $({\rm n} = 0, \pm 1, ...)$ . Setting

$$G(\underline{t},\underline{r}';\nu,k_{zo}) = \sum_{m,n=-\infty}^{\infty} g_{mn}(\rho,\rho';\nu,k_{zo}) \Phi_{mn}(\phi,z) \Phi_{mn}^{*}(\phi',z')$$
(6a)

one finds from Eq. (2a) that the radial Green's functions  $\mathbf{g}_{\mathbf{mn}}(\boldsymbol{\rho},\,\boldsymbol{\rho}')$  obey

$$\frac{1}{\rho} \frac{d}{d\rho} \left( \rho \frac{dg_{mn}}{d\rho} \right) + \left( \kappa_n - \frac{\nu_m}{\rho^2} \right) g_{mn} = -\frac{\delta(\rho - \rho')}{\rho} . \tag{6b}$$

To satisfy Eq. (2b), one requires  $g_{mn}(a, \rho^*) = 0$ , and to insure Eq. (2c),  $g_{mn}(\rho, \rho^*)$  must have the form of an outgoing wave, or decay as  $\rho \to \infty$ . With square root choice Re  $[k_n] = \text{Re} [(k^2 - k_{2n}^2)^{1/2}] > 0$ , and Im  $[k_n] \leqslant 0$ , the solution for  $g_{mn}$  is

$$g_{mn}(\rho,\rho') = \frac{\pi}{2i} H_{\nu_m}^{(2)}(\kappa_n \rho_{>}) Z_{\nu_m}(\kappa_n \rho_{<})$$
 (7a)

with

$$Z_{\nu_m}(\kappa_n \rho_<) = J_{\nu_m}(\kappa_n \rho_<) - \frac{J_{\nu_m}(\kappa_n a)}{H_{\nu_m}^{(2)}(\kappa_n a)} H_{\nu_m}^{(2)}(\kappa_n \rho_<)$$
 (7b)

and  $\rho_{>(<)}$  = max (min) ( $\rho$ ,  $\rho$ ). The  $J_{\nu}$  and  $H_{\nu}$  denote Bessel functions of the first kind and Hankel functions of the second kind, both of order  $\nu_{m}$ .

The forced dipole excitation implies a prescribed gap voltage  $V_g$  and the associated gap electric field  $E_g = E_g z_0$ , such that  $V_g = -E_g h$ .

The boundary conditions on the dipole surface,  $\mathbf{E}_{\mathbf{z}} = 0$  on the dipole arms and  $\mathbf{E}_{\mathbf{z}} = \mathbf{E}_{\mathbf{g}}$  in the gap, lead via Eqs. (1) and (3a) to a linear integral equation of the first kind for the unknown dipole current density (assumed to also flow through the gap):

$$\frac{\hat{\mathbf{G}}}{\mathbf{K}} = \int_{\mathbf{S}} \hat{\mathbf{G}}(\underline{\mathbf{r}},\underline{\mathbf{r}}') \ \mathbf{K}(\underline{\mathbf{r}}') \ d\mathbf{S}' = \begin{cases} \mathbf{0} \ \text{on dipole arms} \\ \mathbf{E}_{\mathbf{g}} \ \text{in the gap} \end{cases}$$
 (8a)

where

$$\hat{\mathbf{G}}(\underline{\mathbf{r}},\underline{\mathbf{r}}') = -\frac{\mathbf{j}\omega\mu_0}{\mathbf{k}^2} \left(\frac{\partial^2}{\partial z^2} + \mathbf{k}^2\right) \mathbf{G}(\underline{\mathbf{r}},\underline{\mathbf{r}}') . \tag{8b}$$

The integral Eq. (8a) is solved approximately via Galerkin's procedure by first expanding K(r') in the form

$$K(\underline{\mathbf{r}}') = \sum_{\mathbf{q}=1}^{\mathbf{q}=1} \mathbf{c}_{\mathbf{q}} \ \Psi_{\mathbf{q}} (\phi', \mathbf{z}') \tag{9}$$

in terms of a finite set of linearly independent basis functions  $\psi_q$ , such that  $\psi_q(\phi^*, z^*) = 0$  for  $|\phi^*| > w/2\rho_0$ ,  $|z^*| > L/2$ ,  $\psi_q(\phi^*, z^*) = \psi_q(z^*)$  for  $|\phi^*| < w/2\rho_0$ ,  $|z^*| < L/2$  and  $\psi_q(\phi^*, L/2) = \psi_q(\phi^*, -L/2) = 0$ , where we have assumed a uniform current density across the dipole's narrow dimension. Using Eq. (%a) in Eq. (8a), one has, in operator form,

$$\sum_{q=1}^{Q} c_q \hat{\underline{G}} \underline{\Psi}_q = E_g \underline{p}_h \underline{p}_w$$
 (10)

where  $p_h = p_h(z')$  and  $p_w = p_w(\phi')$  represent, respectively, a unit pulse of width h centered at z'' = 0, and of width w centered at  $\phi'' = 0$ . Relation (10) is enforced by taking its moments with each of the  $\psi_q$ . This procedure yields the desired set of linear, inhomogeneous equations for the unknown set of  $c_q$ , that is,

$$\sum_{q=1}^{Q} c_{q} \left( \underline{\Psi}_{p}, \underline{\hat{G}} \underline{\Psi}_{q} \right) = E_{g} \left( \underline{\Psi}_{p}, \underline{p_{h}p_{w}} \right) \qquad (p = 1, 2, ..., P = Q). \tag{11}$$

The inner (scalar) product is (f, g) defined by

$$\frac{w/2\rho_0}{(\underline{f},\underline{g})} = \int_{-w/2\rho_0}^{w/2\rho_0} d\phi \int_{-L/2}^{L/2} f(\phi,z) g(\phi,z) dz .$$

$$(12)$$

Explicitly, Eq. (11) reads

$$-\frac{\pi \zeta k \rho_{o}}{2} \sum_{q=1}^{Q} c_{q} \sum_{m,n=-\infty}^{\infty} \left(\frac{\kappa_{n}}{k}\right)^{2} H_{\nu_{m}}^{(2)}(\kappa_{n}\rho_{o}) Z_{\nu_{m}}(\kappa_{n}\rho_{o}) (\underline{\Psi}_{p'},\underline{\Phi}_{mn}) (\underline{\Psi}_{q'},\underline{\Phi}_{mn}^{*})$$

$$= \mathbf{E_g} \left( \underline{\Psi}_{\mathbf{p}}, \underline{\mathbf{p_h}} \mathbf{p_w} \right) \tag{13}$$

with  $\zeta = (\mu_0/\epsilon_0)^{1/2} = 120\pi \Omega$ . Choosing

$$\Psi_{q} = \sin \frac{q\pi}{L} (z + \frac{L}{2}), \ q = 1, 2, ..., Q, \ |z| \le \frac{L}{2}, \ |\Phi| \le \frac{w}{2\rho_{0}}$$
 (14a)

one finds

$$(\underline{\Psi}_{\mathbf{q}}, \underline{\Phi}_{\mathbf{mn}}^*) = \frac{\mathbf{w}\pi \mathbf{L}}{\rho_0 \sqrt{\alpha \mathbf{d}}} \, \mathbf{S}_{\nu_{\mathbf{m}}} \, \mathbf{C}_{\mathbf{nq}}^* \tag{14b}$$

where

$$s_{\nu_{m}} = \frac{\frac{\nu_{m}w}{2\rho_{o}}}{\frac{\nu_{m}w}{2\rho_{o}}} \tag{14e}$$

and

$$C_{nq} = \frac{q[(-1)^{q_1}e^{-j\frac{k_{2n}L}{2}} - e^{j\frac{k_{2n}L}{2}}]}{(k_{2n}L)^2 - (q_{77})^2} . \tag{34d}$$

Furthermore,

$$(\underline{\Psi}_{p}, \underline{p_{h}p_{w}}) = \int_{-w/2p_{w}}^{w/2p_{w}} d\phi \int_{-h/2}^{h/2} \sin \frac{p\pi}{L} (z + \frac{L}{2}) dz = \frac{wh}{p_{w}} B_{p}$$
(15a)

where

$$B_{p} = \sin \frac{p\pi}{2} \frac{\sin \frac{p\pi h}{2h}}{p\pi h}.$$
 (156)

Substitution of Eqs. (14) and (15) into Eq. (13) yields the following system of librarinhomogeneous equations for the determination of the unknown dipole current expansion coefficients:

$$\sum_{q=1}^{\infty} A_{pq} (\hat{c}_{qw}) = B_{p} \qquad (p = 1, 2, ..., P = Q)$$
 (186a)

where

$$A_{pq} = \sum_{m,n=-\infty}^{\infty} \left( \frac{\kappa_n}{k} \right)^2 H_{\nu_m}^{(2)} (\cdot_n \rho_0) Z_{\nu_m} (\kappa_n \rho_0) S_{\nu_m}^2 C_{np} C_{nq}^*$$
 (16b)

and

$$\hat{c}_{q} = c_{q} \frac{NkL^{2}\pi^{2}\zeta}{4dV_{q}} . \qquad (16c)$$

#### 2.3 Active Gap-Impedance

Once the dipole current density K(z) has been arrived at, the active gap-impedance is determined via

$$Z_g(\nu, k_{20}) = \frac{V_g}{\langle l_g \rangle} = \frac{-E_g h}{\frac{w}{h} \int_{-h/2}^{h/2} K(z) dz}$$
 (17)

where  $\langle I_g \rangle$  denotes the average gap current. Substituting Eq. (10a) into Eq. (17) using Eq. (16c), one has

$$Z_{g}(\nu, k_{zo}) = R_{g}(\nu, k_{zo}) + j X_{g}(\nu, k_{zo}) = \zeta \frac{N\pi^{2}L^{2}k}{4d \sum_{q \ge 1} (\hat{c}_{q}w) B_{q}}.$$
 (18)

#### 2.4 Matching Network and Reflection Coefficient

For a good radiation efficiency, an identical network is incorporated in each TEM feed-line to match the dipole impedance  $Z_g$  for a selected pair of values of  $\nu$  and  $k_{z0}$ . This lossless reciprocal two-port network is characterized by its scattering matrix  $\underline{S}$ . It is defined between the reference planes on the input and output transmission lines with characteristic impedances  $Z_1$  and  $Z_2$  and is illustrated in Figure 3. Three specific forms of matching networks including derivation of respective S-parameters are discussed in Appendix D.

With the aid of Figure 3, one can determine the active reflection coefficient  $\Gamma_1$  at the input to the matching network to be (see Section 2, Appendix D)

$$\Gamma_{1}(\nu, k_{zo}) = \frac{S_{11} - \Delta \Gamma_{2}(\nu, k_{zo})}{1 - S_{22} \Gamma_{2}(\nu, k_{zo})}$$
(19a)

where  $\Delta = S_{11}S_{22} - S_{12}S_{21}$ 

$$\Gamma_2(\nu, k_{20}) = \Gamma_0(\nu, k_{20}) e^{-j2\beta_2 \ell_2}$$
 (19b)

and

$$\Gamma_g(\nu, k_{20}) = \frac{Z_g(\nu, k_{20}) - Z_2}{Z_g(\nu, k_{20}) + Z_2}$$
 (19c)

is the unmatched, active gap reflection coefficient. In Eq. (19b),  $\beta_2$  and  $\lambda_2$  denote the propagation constant and the length of the output transmission line.

The voltage  $V_{\mathbf{g}}$  across the gap is given by Eq. (D14) as

$$V_{g}(\nu, k_{zo}) = \frac{S_{21}[1 + \Gamma_{g}(\nu, k_{zo})]}{1 - S_{zz} \Gamma_{z}(\nu, k_{zo})} e^{-j2\beta_{z}\ell_{z}} V_{inc}.$$
 (30)

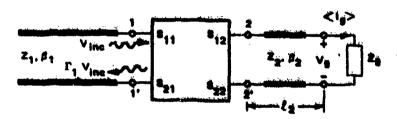


Figure 3. Equivalent Network for a Dipole Element in a Cylindrical Array

#### 2.5 Active Array Fields

From Eqs. (3a), (1), (6a), and (7b), one finds for  $p>p_0$  the said component of the electric field of the active array

$$E_{z}(\nu, k_{zo}) = -\frac{\zeta \pi k \rho_{o}}{2} \sum_{m,n=-\infty}^{\infty} \left(\frac{\kappa_{n}}{k}\right)^{2} H_{\nu m}^{(2)}(\kappa_{n}\rho)$$

$$Z_{\nu m}(\kappa_{n}\rho_{o}) \sum_{n=1}^{\infty} o_{q}(\underline{\Psi}_{q},\underline{\Phi}_{mn}^{*}) \underline{\Phi}_{mn}. \tag{21}$$

Utilizing Eqs. (14b), (15d), (19) and the relations  $N=2\pi/\alpha$ ,  $b=\alpha\rho_0$ , Eq. (21) can be cast into the form

$$E_{z}(\nu, k_{z0}) = \frac{V_{inc}}{\sqrt{bd}} \sum_{m,n=-\infty}^{\infty} T_{mn}(\nu, k_{z0}) H_{pm}^{(z)}(\kappa_{n}\rho) e^{-j(\nu_{m}\phi + k_{z0}z)}$$
(334)

where the active transmission coefficient is

$$T_{mn} (\nu, k_{20}) = -\frac{16d}{\pi L} \frac{V_g (\nu, k_{20})}{V_{inc}} \left(\frac{\kappa_n}{k}\right)^2 Z_{\nu_m} (\kappa_n \rho_0) S_{\nu_m} \sum_{q=1}^{Q} (\hat{g}_q w) C_{nq}^{\pm}. \tag{22b}$$

#### 2.6 Element Pattern

In view of the identity

$$\delta_{oe} \delta_{ot} = \frac{d}{2\pi N} \sum_{\mu=0}^{N-1} e^{-j\mu} \frac{2\pi}{N} \int_{-\pi/d}^{\pi/d} e^{-jk_{zo}dt} dk_{zo} \qquad (8 = 0,1,...,N-1)$$

$$(23a)$$

where  $\delta_{0s}$  and  $\delta_{0t}$  denote the Kronecker deltas, the expression for  $E_{2}^{(e)}$  due to the singly excited (s = 0, t = 0) element becomes

$$\mathsf{E}_z^{(e)}(t) = \frac{\mathsf{fbd}}{4\pi^2 \rho_e} \, \mathsf{V}_{\mathsf{inc}} \, \sum_{\mathsf{pro}}^{\mathsf{N-1}} \sum_{\mathsf{manne}}^{\mathsf{manne}} e^{-\mathsf{j} \mathsf{p}_{\mathsf{m}} \varphi}$$

$$\sum_{n=-\infty}^{\infty} \int_{-\pi/d}^{\pi/d} T_{mn} (r, k_{mn}) H_{mn}^{(2)} (\kappa_{mn}) e^{-ik_{mn}z} dk_{mn}.$$
 (23b)

Transforming the integration variables  $k_{gn} = k_{g0} + 2\pi n/d - k_{g}$ , one finds

$$E_{z}^{(e)}(r) = \frac{\sqrt{bd}}{4\pi^{2}\rho_{0}} V_{inc} \sum_{\nu=0}^{N-1} \sum_{m=-\infty}^{\infty} e^{-j\nu_{m}\phi}$$

$$\frac{\pi}{d} + \frac{2\pi}{d} n$$

$$\sum_{n=-\infty}^{\infty} \int T_{mo}(\nu, k_{z}) H_{\nu m}^{(2)}(\kappa \rho) e^{-jk_{z}z} dk_{z}$$

$$-\frac{\pi}{d} + \frac{2\pi}{d} n$$
(24)

where  $\kappa = (k^2 - k_z^2)^{1/2}$  and where the Floquet relation  $T_{mn}$  ( $\nu$ ,  $k_{z0}$ ) =  $T_{m0}$  ( $\nu$ ,  $k_{zn}$ ) has been invoked. The sum over the index n in Eq. (24) may be further converted into an infinite integral so that

$$E_{z}^{(e)}(r) = \frac{\sqrt{bd}}{4\pi\rho_{o}} V_{inc} \sum_{\nu=0}^{N-1} \sum_{m=-\infty}^{\infty} e^{-j\nu_{m}\phi} \int_{-\infty}^{\infty} T_{mo}(\nu,k_{z}) H_{\nu_{m}}^{(2)}(\kappa\rho) e^{-jk_{z}z} dk_{z}. (25)$$

Using the first term of the large-argument asymptotic expansion for  $H_{\nu_m}^{(2)}(\kappa_{\rho})$ , the far field becomes

$$E_z^{(n)}(r) \sim \frac{\sqrt{nd}}{4\pi\rho_0} V_{inc} e^{i\frac{\pi}{4}} \sum_{\nu=0}^{m} \sum_{m=-\infty}^{m} e^{-j\nu_m(\phi-\frac{\pi}{4})} I_m(\nu;\rho,z)$$
 (26a)

with

$$I_{m}(\nu;\rho,z) = \int_{-\infty}^{\infty} \sqrt{\frac{2}{\pi\kappa\rho}} T_{mo}(\nu,k_{z}) e^{-j(\kappa\rho+kz)} dk_{z}. \qquad (36b)$$

The integral in Eq. (26b) is evaluated by the stationary phase method. Setting  $k_z$  = k cos u,  $\rho$  = r sin  $\theta$ , z = r cos  $\theta$ , where  $\theta$  is measured from the cylinder axis, one may write

$$\kappa \rho + k_z z = kr \cos(u - \theta) \tag{27}$$

which results in a relevant saddle point  $u^{(g)} = \theta$ , and, consequently,  $k_g^{(g)} = k \cos \theta$ . The first-order stationary phase evaluation of the integral  $l_{gg}$  ( $\nu; \rho$ , z) yields

$$I_{m}(\nu \cdot \rho, z) = 2 T_{me} (\nu, k \cos \theta) \frac{1}{2} \frac{(w - \frac{\pi}{4})}{4}$$
 (88)

From Eqs. (26a), (26b), and (28), one has

$$E_{\theta}^{(n)}(t) = \frac{E_{\theta}^{(n)}(t)}{\sin \theta} \sim \frac{1}{\lambda} \sqrt{\frac{1}{2_{\eta}}} V_{\text{inc}} \frac{e^{-jk\tau}}{\tau} P(\theta,\phi)$$
 (25a)

where

$$F(\theta,\phi) = \frac{1}{\pi k \rho_0 \sin \theta} \sqrt{\frac{Z_1}{\zeta}} \sum_{\nu=0}^{d-1} \sum_{m=-\infty}^{\infty} T_{mo} \left(\nu, k \cos \theta\right) e^{-i\nu_m \left(\phi - \frac{\pi}{2}\right)}. \tag{29b}$$

it turns out that the lowest order term of  $E_{\phi}$  is  $O \sim (1/r^2)$ , so that the  $E_{\phi}$  contribution to the far field may be emitted, and, consequently,  $E_{\phi}$  constitutes the entire far electric field due to a singly excited dipole element in a match-terminated array environment. The realized element gain pattern

$$G_{\theta}^{(e)}(\theta,\phi) = \frac{\left|\mathbb{E}_{\theta}^{(e)}(\theta,\phi)\right|^{2}}{\left(\frac{P_{los}}{4\pi\tau^{2}}\right)}$$
(30a)

defined with respect to the available power  $P_{inc} = |V_{inc}|^2/Z_1$  may now be written as

$$G_{\theta}^{(o)}(\theta,\phi) = 4\pi \frac{bd}{\lambda^2} |F(\theta,\phi)|^2. \tag{30b}$$

Denoting the complex field element pattern by

$$g_{\theta}^{(\bullet)}(\theta,\phi) = \sqrt{4\pi \frac{bd}{\lambda^2}} F(\theta,\theta)$$
 (31a)

Eq. (29a) can be expressed in the form

$$E_{\theta}^{(e)}(r,\theta,\phi) = \sqrt{\frac{\zeta}{4\pi Z_1}} V_{inc} \frac{e^{-jkr}}{r} g_{\theta}^{(e)}(\theta,\phi) . \tag{31b}$$

#### 3. ANALYSIS FOR ISOSCELES TRIANGULAR LATTICE

#### 3.1 Array Model

The dipoles are now arranged in an isosceles triangular lattice as shown in Figure 4. This lattice may be generated from a rectangular one, for example, by displacing every other ring by  $\pi/N$  rad in the angular direction. The location of the array elements on a cylindrical surface of radius  $\rho_0$  is defined by the skewed curvilinear basic vectors (see Figure 4)

$$\underline{p}_{st} = s\underline{p}_1 + t\underline{p}_2$$
, (s = 0, 1,..., N - 1; t = 0, ±1,...), (32)

where t indicates the ring and s the element number in it. The center of the singly excited element (s = 0, t = 0) is located at ( $\rho_0$ ,  $\phi$  = 0, s = 0). The extent of a wedge-shaped unit cell of rectangular cross section is  $2\pi/N \times 2d$  as indicated in Figure 4.

### 3.2 Active Gap-Impedance and Reflection Coefficient

The analysis exploits the previously obtained results for a rectangular grid geometry. In particular, the expansion of the unit cell Green's function as given in Eq. (6a) also applies here with the proviso that the double sum it lices are constrained to (m + n) of even parity as demonstrated in Appendix A. Consequently, the relevant expressions for active impedances and reflection coefficients in an

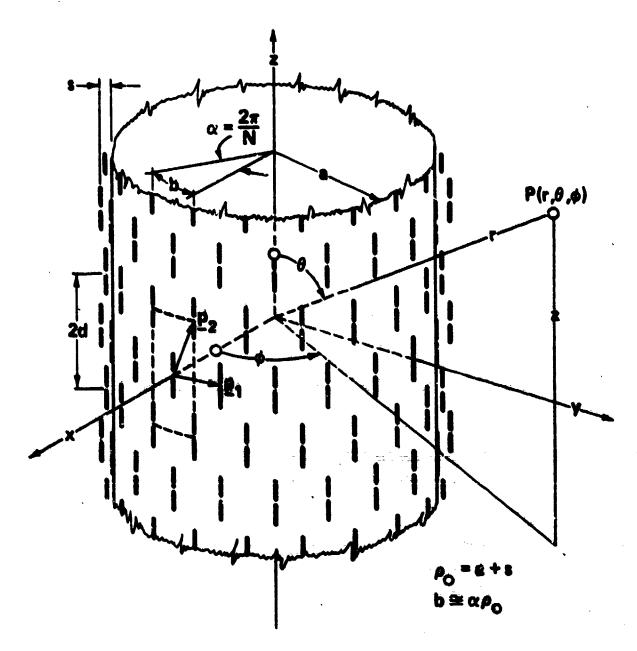


Figure 4. Geometry of the Circular Cylindrical Array of Dipoles in a Triangular Lattice

isosceles triangular lattice can be simply inferred from the solution for the corresponding rectangular grid array by restricting the summation in Eq. (6a) to (m+n) even. With this proviso implemented in Eq. (16b), the system of linear equations (16a) is also valid for isosceles triangular lattices. Thus, with this modification, the relations of Sections 2.3 and 2.4 apply to cylindrical dipole arrays with isosceles triangular lattices.

#### 3.3 Element Pattern

A single (s = 0, t = 0) array element excitation in an isosceles triangular lattice of Figure 4 can be expressed in terms of an excitation vector  $\mathbf{a} = \{\delta_{s0}\delta_{t0}\}$  (s = 0, 1,..., N = 1; t = 0, ±1,...). In Appendix B, the following identity is demonstrated:

$$\delta_{so} \ \delta_{to} = \frac{d}{4\pi N} \sum_{\nu=-N}^{\nu=-N} e^{-j\nu \left(\frac{2N}{N}a + \frac{N}{N}t\right)} \int_{-\pi/d}^{\pi/d} e^{-jk_{so}dt} \ dk_{so} \ . \tag{33}$$

Each term in Eq. (33) under the sum and integral signs represents a unit-amplitude progressive-phase array excitation,  $2\pi\nu/N$  rad in angular direction and  $k_{z0}d + \pi\nu/N$  rad in the skew direction. In view of Eq. (33), the electric field due to the singly excited dipole element in a triangular lattice environment is

$$\underline{\mathbf{E}^{(o)}}(\mathbf{r}) = \frac{\mathbf{d}}{4\pi N} \sum_{\nu = -N}^{N-1} \int_{-\pi/d}^{\pi/d} \underline{\mathbf{E}}(\mathbf{r}; \nu, \mathbf{k}_{20}) d\mathbf{k}_{20}$$
 (34a)

where, from Eq. (22a)

$$E_{z}(\underline{r}; \nu, k_{zo}) = \frac{V_{inc}}{\sqrt{bd}} \sum_{m,n=-\infty}^{\infty} T_{mn}(\nu, k_{zo}) H_{\nu m}^{(2)}(\kappa_{n}\rho) e^{-J(\nu_{m}\phi + k_{zo}Z)}$$
(34b)

and  $T_{mn}$  is given by Eq. (22b). Following the procedure of Section 2.6, one can readily show that the expressions for element pattern and far field are identical to those of Eq. (31), where now

$$F(\theta,\phi) = \frac{j}{\pi k \rho_0 \sin \theta} \sqrt{\frac{Z_1}{\zeta}} \sum_{\nu=-N}^{N-1} \sum_{m=-\infty}^{\infty} T_{2m,0}(\nu,k\cos\theta) e^{-j\nu_{2m}(\phi-\frac{\pi}{2})}$$
(35)

and  $T_{2m, 0}$  is given by Eq. (22b) with n = 0 and  $k_{z0} = k \cos \theta$ .

#### 4. NUMERICAL ANALYSIS

Based on the above analysis, a Fortran IV computer program was generated for evaluation of the phase sequence active gap-impedances, of the phase sequence active reflection coefficients at the input to the matching network, and of the element pattern for both rectangular and isosceles triangular lattice configurations.

#### 4.1 Rectangular Lattice

The dipole current expansion coefficients  $c_q$  [see Eq. (9)] were computed from Eq. (16a), where Q is the number of current terms. The (Q x Q) matrix in Eq. (16a), with the elements A  $_{pq}$  as given by Eq. (16b), is Hermitian, that is, A  $_{pq}$  = A $_{qp}$ , and, therefore, only Q(Q + 1)/2 matrix coefficients need be evaluated. Furthermore, one observes that the A $_{pq}$  and, consequently,  $c_q$ , as well as the gap impedances  $Z_g(\nu, k_{g0})$  and the reflection coefficients  $\Gamma_1(\nu, k_{g0})$ , are even functions of  $\nu$ . This result follows, for instance, for A $_{pq}$ , by first performing a change of variables  $\nu \rightarrow \nu$ -(N - 1)/2 for N odd and  $\nu \rightarrow \nu$ - N/2 for N even. As a result,  $\sum_{\nu=0}^{N-1} \rightarrow \sum_{\nu=-(N-1)/2}^{(N-1)/2}$  for N odd and  $\sum_{\nu=0}^{N-1} \rightarrow \sum_{\nu=-N/2}^{N/2-1}$  for N even. From Eq. (16b), it is now obvious, upon replacing  $\nu$  by  $-\nu$  and simultaneously m by -m, that  $A_{pq}(\nu) = A_{pq}(-\nu)$ .

The Bessel and Hankel functions in expressions for  $A_{pq}$  were evaluated by the usual numerical methods, <sup>7</sup> each applicable in its own range of validity with respect to the argument and order. To avoid numerical overflow or underflow in regions where asymptotic expansions apply, the Bessel and Hankel functions were not calculated separately but, instead, an asymptotic expression for  $Z_{\nu m}H_{\nu m}^{(2)}$  was employed as described in Appendix E. In this fashion, the exponential dependence of the individual factors has been suppressed.

The double sum in Eq. (16b) was evaluated in the form  $\Sigma_n s_n$  ( $\Sigma_m f_{min}$ ). With respect to the rate of convergence of the series in Eq. (16b), the following observations are relevant: The series  $\Sigma_n$  converges as  $1/n^3$ . Since  $w/2\rho_0 \ll 1$  in the factor  $S_{\nu_m}$  as given by Eq. (14c), the rate of convergence of  $\Sigma_m$  is predominantly determined by the large m behavior of  $Z_{\nu_m} H_{\nu_m}^{(2)}$  which is  $1/\pi |m|$  N. The slow convergence of this series with respect to the angular index m was accelerated as described in Appendix C. With such convergence acceleration and with the nine-significant-digit accuracy of the Bessel functions, a numerical accuracy to five significant figures in  $Z_g(\nu,k_{g0})$  was obtained for ka = 120, using modal indices in and n between  $\pm 10$ .

The set of equations (16a) was solved using Gauss's elimination method. It should also be mentioned that for  $\theta = \pi/2$  ( $k_{20} = 0$ ), that is, in the principal H-plane cut of the element pattern, the axial dipole current density is reflection-symmetric with respect to the dipole center. For an arbitrary phasing  $k_{20}$ , that is, for a conical cut with  $\theta \neq \pi/2$ , odd terms also appear in the series Eq. (10a). However, the resulting asymmetry is relatively minor, since the magnitudes of

<sup>7.</sup> Abramowitz, M., and Stegun, I. (1964) Handbook of Mathematical Functions, U.S. Dept. Commerce, Nat. Bur. Stand.

even (q) dipole current terms are much smaller than the odd (q) ones. This feature is due to the constant gap E-field assumption.

Using the known dipole current coefficients, the active gap-impedances  $Z_g(\nu, k_{z0}) = R_g(\nu, k_{z0}) + jX_g(\nu, k_{z0})$  were calculated from Eq. (18). Figure 5 shows the "broadside scan" gap-resistance  $R_g(0, 0)$  versus the number of dipole current terms for three dipole lengths,  $L = 0.4\lambda$ ,  $L = 0.5\lambda$ , and  $L = 0.6\lambda$ . The respective reactances  $X_g(0, 0)$  are seen in Figure 6. Since, in this case, the even dipole current terms are not excited, they are not shown in Figures 5 and 6. One observes that for short dipole lengths, a single current term yields a good approximation to the dipole impedance. It was found that the curves  $Z_g(\nu > 0, k_{z0} > 0)$  versus Q exhibit a similar behavior as  $Z_g(\nu = 0, k_{z0} = 0)$  shown above.

The relative convergence phenomenon was observed by monitoring the behavior of current expansion coefficients and active gap-impedance values as a function of the number of unit cell modes n and the number of current terms Q. It was found that, for a stable solution, it is necessary to impose the condition  $Q < 2Ln_{max}/d$ . For example, if  $n_{max} = 15$  and d = 0.7, one requires Q < 17 if  $L = 0.4\lambda$ ,  $Q \le 21$  if  $L = 0.5\lambda$ , and  $Q \le 25$  if  $L = 0.6\lambda$ . If Q increases beyond these values, the numerical values for  $Z_{\sigma}$  tend to become progressively less accurate, as can be seen from Figures 5 and 6. This condition on Q insures an adequate resolution of the dipole current distribution in terms of the unit cell Floquet mode basis. Therefore, the highest axial spatial frequency of the truncated unit cell mode basis  $2\pi n_{max}/d$  should be greater than the highest spatial frequency  $Q\pi/L$  of the dipole current basis. If a high degree of accuracy in  $Z_{\sigma}$  is desired, that is, when more current terms are needed, one must also increase n and  $m_{max}$ , respectively. The reason for the increase of  $m_{max}$  along with  $n_{max}$  is the behavior of the Bessel's functions in Eq. (16b). Namely, with increasing  $n_{max}$ , the arguments of the  $Z_{\nu_m}(\kappa_n; a, \rho_0)$  and of  $H_{\nu_m}^{(2)}(\kappa_n \rho_0)$  increase. Therefore, to achieve a sufficient accuracy in  $A_{pq}$ , it is necessary to increase  $\nu_{m}$  past the transition region, that is,  $\nu_m > |\kappa_n \rho_0|$ , where the convergence of the series may be accelerated as described in Appendix C.

The active reflection coefficients  $\Gamma_1(\nu, k_{20})$  at the input port of the matching network were computed from Eq. (19a). Two simple matching networks have been considered: (a) series and (b) parallel, both shown in Figure 7. In each case,  $k_2 = 0$  and network parameters have been chosen so as to match the active cylindrical array at  $\nu = 0$  and  $k_{20} = 0$  (see Figure 3). In Figure 7, the transformer

<sup>8.</sup> Lee, S. W., Jones, W.R., and Campbell, J.J. (1970) Convergence of numerical solution of iris-type discontinuity problems, Antennas Propag. Symp. Dig., Ohio State University, Columbus.

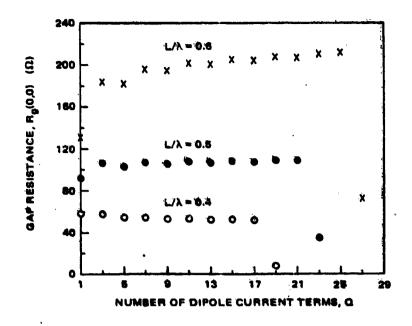


Figure 5. Gap-Resistance  $R_g(0, 0)$  Versus Number of Dipole Current Terms  $(b/\lambda = 0.6, d/\lambda = 0.7, s/\lambda = 0.25, w/\lambda = 0.05, h/\lambda = 0.01)$ 

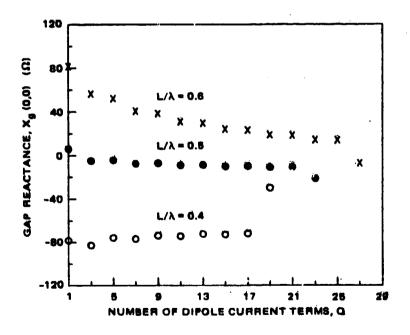


Figure 6. Gap-Reactance  $X_g(0, 0)$  Versus Number of Dipole Current Terms (b/ $\lambda$  = 0.6, d/ $\lambda$  = 0.7, s/ $\lambda$  = 0.25, w/ $\lambda$  = 0.05, h/ $\lambda$  = 0.01)

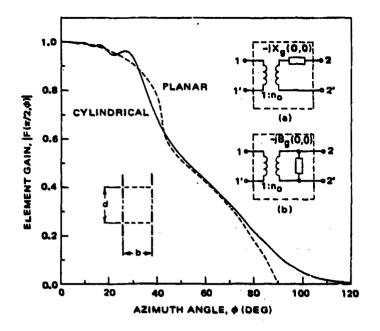


Figure 7. H-Plane Voltage Element Gain Pattern for Cylindrical and Reference Planar Arrays and Matching Networks. (a) Series, (b) Parallel (b/ $\lambda$  = 0.6, d/ $\lambda$  = 0.7, ka = 120)

ratio  $n_0 = (R_g(0, 0)/Z_1)^{1/2}$  in case (a), and  $n_0 = (Y_1/G_g(0, 0)^{1/2}$  in case (b), where  $Y_g(\nu, k_{z0}) = 1/Z_g(\nu, k_{z0}) = G_g(\nu, k_{z0}) + jB_g(\nu, k_{z0})$ .

The element patterns of the excited element located at  $(\rho_0, \theta = 90^\circ, \phi = 0^\circ)$  were calculated in the spherical coordinate system  $(r, \theta, \phi)$ , having its z-axis coincident with that of the cylinder according to the relations in Eqs. (31) and (29b).

#### 4.2 Triangular Lattice

The steps in Section 4.1 apply also to a triangular lattice. The dipole current density expansion coefficients are again computed from Eqs. (16a) and (16b) but with (m + n) even. The convergence of the series in Eq. (16b) was accelerated as described in Appendix C. Because the axial unit cell dimension is 2d (see Figure 4), the relative convergence condition is  $Q < Ln_{max}/d$ . The element patterns were calculated from Eq. (31) using Eq. (35).

The program was run on a CDC 6600 computer at the Courant Institute of Mathematical Science, New York University, N.Y., and at the AFGL Computer Center, Hanscom AFB, Mass. All calculations were carried out in single precision (15 significant digits on a CDC 6600 computer) complex arithmetic. The execution time for a 180-point element pattern is less than one minute. The memory required for this program is 150 kbytes.

#### 5. NUMERICAL RESULTS AND DISCUSSION

The amplitude and phase of the element patterns were computed for representative values of array parameters, and the results are grouped to exhibit the significant trends. The numerical results stress the element performance aspects relevant to cylindrical array design.

In order to maximize the broadside element gain, a matching network appropriate to in-phase excitation of all dipoles was employed throughout. Except when explicitly stated, the following values of dipole length, width, gap size, and distance to the cylindrical ground were employed, respectively,  $L/\lambda = 0.5$ ,  $w/\lambda = 0.05$ ,  $h/\lambda = 0.01$ , and  $s/\lambda = 0.25$ . In all cases, field amplitude (voltage) element patterns were normalized to the unit cell gain  $(4\pi bd/\lambda^2)^{1/2}$ , and 10 dipole current terms were used in Galerkin's procedure. Most of the numerical results were generated for rectangular grid arrays in conjunction with the design and performance evaluation of the cylindrical array described in Part 2 of this report. They are presented in Figures 7 to 20; those for the triangular lattice appear in Figures 21 and 22. Each is followed by a detailed discussion.

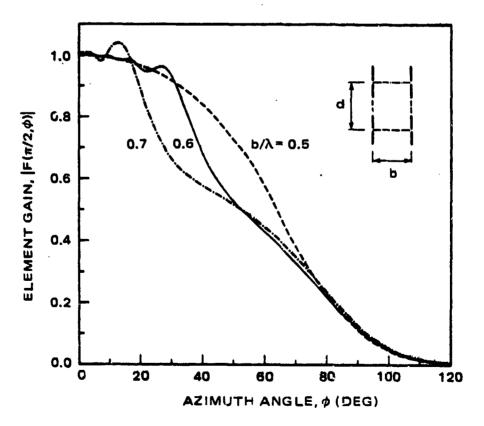


Figure 8. H-Plane Voltage Element Gain Pattern (d/ $\lambda$  = 0.7, ka = 120). Parameter: azimuth spacing b/ $\lambda$  = 0.5, 0.6, 0.7

#### 5.1 Rectangular Grid Array

#### 5.1.1 INFLUENCE OF ARRAY GRID PARAMETERS

#### 5. 1. 1. 1 Element Amplitude Pattern - Forward Region

Figure 7 shows a comparison of the principal H-plane cut ( $\theta = 90^{\circ}$ ) of the voltage element pattern for ka = 120, b/ $\lambda$  = 0.6, d/ $\lambda$  = 0.7 with that of the corresponding planar array. It is observed that both patterns are similar and exhibit a substantial drop-off near  $\phi = 42^{\circ}$ . In the planar array case, this drop-off is caused by an end fire grating lobe condition (EGL) for b/ $\lambda$  = 0.6 and, in the cylindrical array, by its quasiplanar counterpart. As expected, the planar array drop-off is steeper (since, in view of the curvature in the cylindrical array, fewer elements participate in the EGL effect).

Figure 8 illustrates the  $b/\lambda$  dependence of the  $\theta = 90^{\circ}$  cut for ka = 120 and an axial spacing of 0.7 $\lambda$ . It is found that, as in planar arrays, an increase of  $b/\lambda$  causes a predictable progressive narrowing of the element pattern.

The curves of Figure 8 also exhibit a ripple in the broadside region, whose amplitude diminishes with tightening of azimuthal spacing and becomes negligible for  $b/\lambda = 0.5$ . On the other hand, for  $b/\lambda = 0.7$ , one finds a peak-to-peak ripple amplitude of about  $0.5\,\mathrm{dB}$ . In a low sidelobe cylindrical (or curved) array design, it may be necessary to reduce the ripple amplitude and consequently employ a tight azimuthal spacing. More on this subject will be said in Part 2 of this report. The ripple is not an edge effect, as no aperiodic edge discontinuities exist in angularly and axially periodic cylindrical arrays, but is due to the interference of the direct single element radiation (with planar element pattern) with the grating lobes of respective quasiplanar subarrays excited by the guided creeping wave phase gradient, as discussed 1,4 for the case of cylindrical arrays of aperture elements. Since the ripple is a result of a combination of the angular periodicity of the array and its curvature, 1,4 it is also expected to appear, and is, indeed, found in curved periodic dipole arrays.

To exhibit the element pattern features as a function of the elevation angle, Figure 9 shows a number of constant  $\theta$  (conical) cuts for ka = 120, b/ $\lambda$  = 0.6, and d/ $\lambda$  = 0.7. Several trends are observed with decreasing values of  $\theta$  measured from the cylinder axis: The EGL drop-off broadens and shifts toward larger values of  $\phi$ ; the E-plane gain level is progressively reduced, and the ripple amplitude decreases. The first two of these features may be explained in quasiplanar terms and are predictable from the local planar grating lobe diagram adapted for the cylindrical array geometry as shown in Figure 9. In this figure,  $u_{00} = v/ka = \sin \theta_0 \sin \phi_0$  and  $v_{00} = k_{z0}/k = \cos \theta_0$ . As usual, the (m = 0, n = 0) reciprocal lattice point specifies the main beam direction; all other points (m, n) correspond to the grating lobe location in (u, v) space. The (m, n) lobes with  $u_{mn}^2 + v_{mn}^2 < 1$ 

are visible. The amount of shift of EGL drop-off toward larger values of  $\phi$  with decreasing  $\theta$  may be predicted from the geometry of Figure 9, which leads to the relation: \*

$$\sin \phi_{\text{EGL}} = \frac{1}{\sin \theta} \left[ \frac{m}{|m|} \sqrt{1 - \left(\cos \theta + n \frac{\lambda}{d}\right)^2} - m \frac{\lambda}{b} \right]$$

$$(m = 0, \pm 1, ...), (n = 0, \pm 1, ...).$$
(36)

It is seen from Eq. (36) and Figure 9 that in the H-plane ( $\theta$  = 90°), the grating lobe (m = -1, n = 0) enters into real space at  $\phi_{\rm EGL}$  = 42°. As  $\theta$  decreases, the corresponding  $\phi_{\rm EGL}$  shifts toward larger values of  $\phi$ , causing, as already mentioned, a widening of the element pattern. The potential EGL drop-off corresponding to the axial grating lobe (m = 0, n = -1) for  $d/\lambda$  = 0.7, as predicted from Eq. (36) is not noticeable at  $\theta$  = 60,  $\phi_{\rm EGL}$  = 25.4°. The tapering off of the EGL effect with decreasing  $\theta$  and the associated diminishing of the ripple amplitude in Figure 9 are attributed to the reduction of mutual coupling in axial dipole arrays for directions off the principal H-plane, and particularly in the near E-plane region.

Figure 10 shows three E-plane cuts for axial spacings  $d/\lambda = 0.5$ , 0.6, 0.7, with  $b/\lambda = 0.6$  and ka = 120. It was verified (down to ka = 30) that the axial gain roll-off with  $\theta$  matches that in appropriate planar arrays. Although an axial spacing of 0.7 $\lambda$  admits only a limited (to about 23° off broadside) elevation scan of an active array, element patterns for large values of  $\theta$  are useful for sidelobe level evaluation.

Figure 11 exhibits the dependence on cylinder radius (ka) of the EGL drop-off and of the ripple in the  $\theta$  = 90° cut. It is seen that, with decreasing values of ka, the EGL drop-off slope diminishes. Simultaneously, the ripple frequency is reduced and its amplitude increases. The tapering off of the EGL effect is to be expected, since, with decreasing ka, fewer elements participate in its formation. The reduction (with decreasing ka) of the ripple frequency is due to reduction of the creeping-wave grating lobe phase delay variation per unit increment in the observation angle. Finally, the decrease of ripple amplitude with increasing ka is expected due to the increased creeping wave loss. In the planar limit, no ripple is observed.

<sup>\*</sup>This relation can also be obtained from the condition of transition region boundary  $H_{\nu_m}^{(2)}(\kappa_n\rho_0)$ , that is,  $|\nu_m|=\kappa_n\rho_0$ , with  $\nu_0/\kappa_0\rho_0=\sin\theta_0\sin\phi_0$ , and  $k_{2n}/k=\cos\theta_0+n\lambda/d$ .

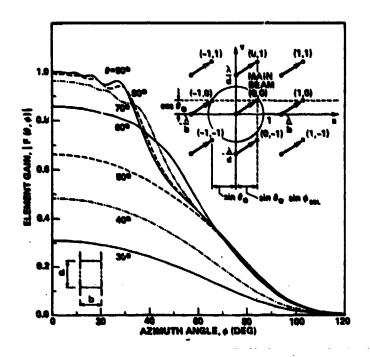


Figure 9. Voltage Element Gain Pattern and Corresponding Local Grating Lobe Diagram (b/ $\lambda$  = 0.6, d/ $\lambda$  = 0.7, ka = 120). Parameter: elevation angle  $\theta$  = 30°, 40°,..., 90°

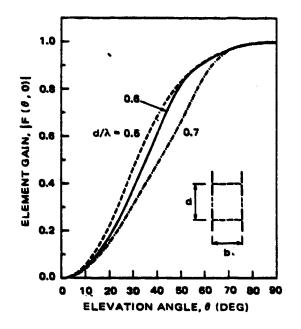


Figure 10. E-Plane Voltage Element Gain Pattern ( $b/\lambda$ = 0.6, ka = 120). Parameter: axial spacing  $d/\lambda$  = 0.5, 0.6, 0.7

#### 5. 1. 1.2 Element Amplitude Pattern-Shadow Region

Knowledge of the shadow region slope is important in the evaluation of far sidelobes. Figure 12 illustrates the dependence on cylinder radius of the shadow region slope, in the  $\theta$  = 90° cut. It is seen that the slope is linear on a dB scale and is found to increase as  $(ka)^{1/3}$ . The linearity of the slope indicates that the angular pattern in the shadow region is primarily due to a single creeping wave contribution with an angular attenuation constant proportional to  $(ka)^{1/3}$ . The ripple in the  $\phi$  = 180° region, similar to that found in the case of an unperforated cylinder, is a result of the interference of two creeping waves traveling in opposite directions around the cylinder. The resolution of this ripple at the very low pattern levels attests to the nigh numerical accuracy of the theory and numerical techniques.

Figure 13 presents the  $\theta$  dependence of the shadow region slope. It is found that in the range of  $\theta$  shown, the slope varies as  $\sin^{1/3}\theta$ . The overall dependence of the shadow region slope on  $(ka \sin \theta)^{1/3}$  is consistent with other asymptotic developments. In all cases, the computed shadow region slope was insensitive to axial spacing.

Figure 14 exhibits the dependence of this slope on azimuthal spacing, for  $d/\lambda = 0.7$ , ka = 120,  $\theta = 90^\circ$ . One observes (see also Figure 8) that the patterns intersect; while the element pattern for  $b/\lambda = 0.5$  is wider in the broadside region, its shadow region slope exceeds that for  $b/\lambda = 0.7$  so that its shadow region element gain falls below that for  $b/\lambda = 0.7$ . This result is not unexpected, because, for smaller values of  $b/\lambda$ , the creeping wave generating the shadow region H-plane pattern encounters a larger density of match-terminated elements. The minor spendence of the E-plane pattern on  $b/\lambda$  is not shown.

#### 5.1,1.3 Element Pattern Phase

Design of a cylindrical arry requires knowledge of the element phase center location. In Appendix F, we describe element phase pattern reference point transformation from array axis to the point ( $\rho_{\rm ph}$ ,  $\theta$  = 90°,  $\phi$  = 0°). Namely, it was found that the flattest element pattern phase in the broadside region is obtained for the phase reference location approximately at ( $\rho_{\rm ph}$  = a + 0.8 s,  $\theta$  = 90°,  $\phi$  = 0°), that is, 0.2 s below the dipole center. Figure 15 exhibits the element pattern phase in the  $\theta$  = 90° cut for the phase reference location at  $\rho_{\rm ph}$ , its dependence on b/ $\lambda$ , for d/ $\lambda$  = 0.7. One observes that the phase varies only by a few degrees up to the EGL drop-off. Thus, the principal H-plane EGL position essentially determines the limit of usefulness of the element, both in amplitude and phase. Figure 16 presents the E-plane element phase pattern versus axial spacing for the choice of parameters of Figure 10.

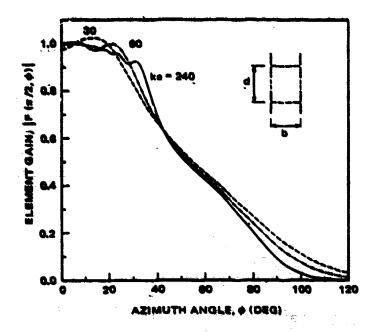


Figure 11. H-Plane Voltage Element Gain Pattern (b/ $\lambda$  = 0.6, d/ $\lambda$  = 0.7). Parameter: cylinder radius ka = 30, 60, 240 (for ka = 120, see Figure 9)

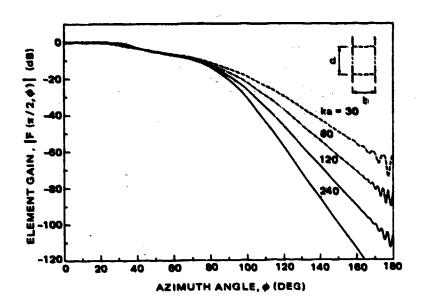


Figure 12. H-Plane Element Gain Pattern (dB) (b/ $\lambda$  = 0.6, d/ $\lambda$  = 0.7). Parameter: cylinder radius ka = 30, 60, 120, 240

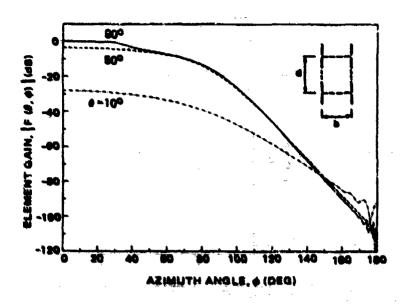


Figure 13. Element Gain Pattern (dB) (b/ $\lambda$  = 0.6, d/ $\lambda$  = 0.7, ks = 120). Parameter: elevation angle  $\theta$  = 10°, 50°, 90°

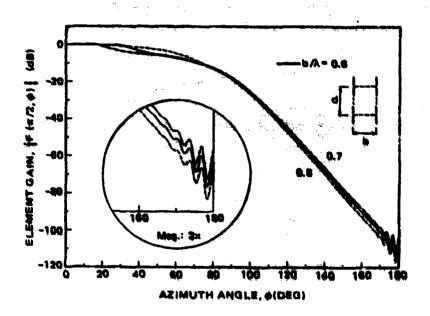


Figure 14. H-Plane Element Gain Pattern (dB)  $(d/\lambda = 0.7, ka = 120)$ . Parameter: azimuth spacing  $b/\lambda = 0.5, 0.6, 0.7$ 

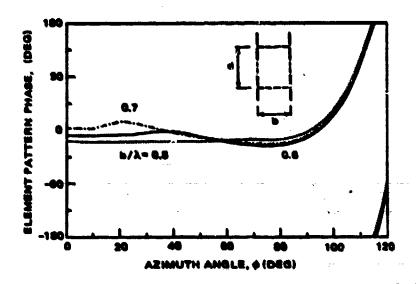


Figure 15. H-Plane Element Phase Pattern (d/ $\lambda$  = 0.7, ka = 120). Parameter: azimuth spacing b/ $\lambda$  = 0.5, 0.6, 0.7

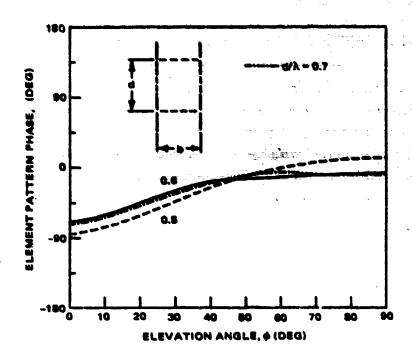


Figure 16. E-Plane Element Phase Pattern (b/ $\lambda$  = 0.6, ka = 120). Parameter: axial spacing d/ $\lambda$  = 0.5, 0.6, 0.7

#### 5.1.2 INFLUENCE OF DIPOLE DIMENSIONS

The influence of the dipole length L and of the distance to ground s on the cylindrical array element pattern was investigated in the  $\theta$  = 90° cut for b/ $\lambda$  = 0.6 and d/ $\lambda$  = 0.7. For each selection of an (L, s) combination, the array was matched for in-phase excitation. The variation of the element gain pattern with L and (or) s, for L/ $\lambda$  = 0.4, 0.5, 0.6, and 0.2  $\leq$  s/ $\lambda$   $\leq$  0.3 was found insignificant. On the other hand, the influence of these parameters on the gap impedance was observed (see Figure 17). It is seen that for L/ $\lambda$  = 0.4, the unmatched broadside gap impedance Z<sub>g</sub>(0, 0) is capacitive; for L/ $\lambda$  = 0.6, it is inductive; while for L/ $\lambda$  = 0.5, Z<sub>g</sub>(0, 0) passes through resonance.

# 5.1.3 FREQUENCY AND SCAN DEPENDENCE

Knowledge of frequency and scan-dependent gap impedance  $Z_g(\nu, k_{g0}; f)$  is needed to design a mulching network. Figure 18 illustrates the frequency and scan dependence of the E- and H-plane gap impedance. The array parameters at center frequency  $f_c$  are  $b/\lambda_c = 0.5$ ,  $d/\lambda_c = 0.6$ ,  $s/\lambda_c = 0.25$ ,  $L/\lambda_c = 0.5$ ,  $h/\lambda_c = 0.01$ . and  $w/\lambda_c = 0.05$  with ka = 120. The active gap-impedance curves  $Z_g(\nu, k_{g0})$  are presented for the three frequencies f = 0.9fc, f = fc and f = 1.1fc. In Figure 18, the gap impedances (normalized to  $Z_0$  = 100Q) are plotted versus elevation scan angle  $\theta_0$  and discrete values of azimuthal scan angles  $\phi_0$ , where  $\cos\theta_0$  =  $k_{\pm 0}/k$ and  $\sin \theta_0 \sin \phi_0 = \nu/ka$ ,  $\nu = 0, 1, ..., N - 1$ . This enables one to compare the scan dependence of the dipole gap-impedance in a cylindrical array with an equivalent infinite planar array. Although  $\mathbf{Z}_{\mathbf{g}}$  depends on both the scan angle and frequency f, it is seen that its variation with  $\phi_0$  is much greater than with f within a ±10 percent frequency band. In a cylindrical phased array, the large scan angle  $\phi_0$  is associated with the edge elements of the excited arc. For broadsidematched elements and a broadside scanned array, these elements will experience a significant impedance mismatch. However, the associated reflection power loss is usually reduced by an amplitude taper of the excitation. The variation of gap impedance versus ( $\theta_0$ ,  $\phi_0$ ) and versus frequency is similar (as one would expect) to that of a corresponding planar array. Figure 19 compares gap impedance  $Z_{g}(\theta_{0} = \pi/2, \phi_{0})$  dependence on  $\phi_{0}$  at  $f = f_{c}$ , for ka = 30 and ka = 120 with those of the equivalent planar array. The Smith chart normalization is in this case  $Z_0 = 500 \Omega$ . A region of overlap ( $\phi_0 = 0^\circ$  to  $50^\circ$ ) may be noticed. For  $\phi_0 > 50^\circ$ curves for ka = 30 first and subsequently those for ka = 120 gradually depart from the planar ones, due to the curvature effect. It was verified that in the E-plane, the values of  $Z_g(\theta_0, \phi_0 = 0^\circ)$  are essentially equal to those of the active impedance of a corresponding planar array down to ka = 30 and are therefore not shown.

Figure 20 illustrates the frequency dependence of the H-plane element pattern. The array was broadside-matched at center frequency  $f_{\rm C}$ . A simple, realistic

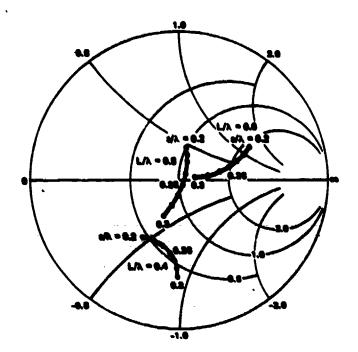


Figure 17. Gap impedance  $Z_g(0, 0)$  Versus Ground Plane Spacing  $(b/\lambda = 0.6, d/\lambda = 0.7, ka = 120, Z_0 = 100Q)$ . Parameter: dipole length  $L/\lambda = 0.4, 0.5, 0.6$ 

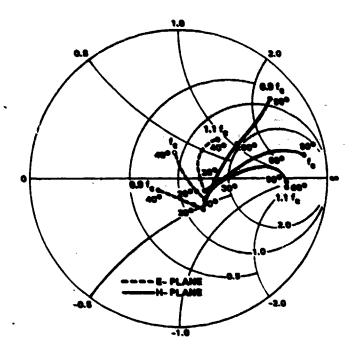


Figure 18. H-Plane Gap-Impedance Versus Asimuth Scan Angle and E-Plane Gap Impedance Versus Elevation Scan Angle Over  $\pm 10$  Percent Frequency Band (b/ $\lambda_{\rm C}$  = 0.5, d/ $\lambda_{\rm C}$  = 0.6, ka = 120,  $Z_0$  = 100 Q)

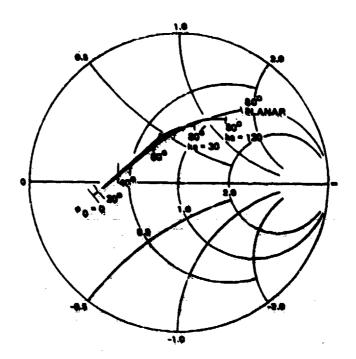


Figure 19. Comparison of Cylindrical and Planar Dipole Array Gap-Impedance for H-Plana Scan (b/ $\lambda_c$  = 0.5, d/ $\lambda_c$  = 0.6, Z<sub>0</sub> = 500 $\mathcal{Q}$ )

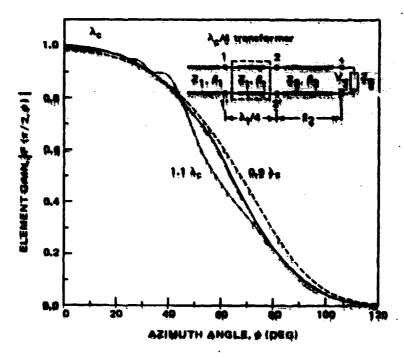


Figure 20. H-Plane Voltage Element Gain Pattern  $(b/\lambda_C \neq 0.5, d/\lambda_C \neq 0.6, ka = 120)$ . Parameter: frequency  $f = 0.0 \ f_{\rm C}$ ,  $f_{\rm C}$ , 1.1  $f_{\rm C}$ 

matching network that consists of a  $\lambda_c/4$  transformer is also shown in Figure 20. The transformer is placed a distance  $\ell_2$  away from the dipole so that the transformed gap impedance at terminals  $(2-2^\circ)$  is real. Since for the given geometry  $Z_g(0, 0) = (137 - j38) \mathcal{Q}$  and  $Z_1 = 50 \mathcal{Q}$ , the value of  $Z_2$  was chosen to be  $Z_2 = 137 \mathcal{Q}$ . As a result,  $\ell_2 = 0.38 \lambda_c$  and  $Z_t = 95 \mathcal{Q}$ . With these (fixed) matching network parameters, the frequency was varied over a  $\pm 10$  percent band. It was observed that the voltage element gain pattern does not change significantly. The pattern shape depends primarily on  $b/\lambda$  as already discussed, while broadside gain decreased 0.2 dB at the end of the band. The curves in Figure 20 can also be obtained (in the lit region) approximately from

$$|F(\frac{\pi}{2}, \phi)| = \sqrt{(1 - |\Gamma_1(\frac{\pi}{2}, \phi)|^2) \cos \phi}$$
 (37)

where  $\Gamma_1$  may be computed from Eq. (19) with the help of Figure 18.

An additional remark is warranted here. It is known that in planar dipole arrays, the feed structure can give rise to E-plane blind spots. These are not predicted by analyses that disregard the influence of the feed structure on radiation. By inference, such blind spots are also expected to appear in cylindrical dipole arrays. Various empirically based remedies can be employed and have been found effective. 9

### 5.2 Triangular Grid

Two isosceles triangular grid geometries were considered. Both grids are derived from a rectangular lattice with  $b/\lambda = 0.6$ ,  $d/\lambda = 0.7$ , and preserve the unit cell area. The first grid (a) is obtained by displacing alternate rings by half the circumferential spacing, the second (b) by shifting alternate columns by half the axial spacing. The two grids produce quite different element patterns.

In the isosceles triangular lattice, for a constant  $\theta$  cut the EGL drop-off, due to an (m, n) grating lobe arriving at the unit circle should appear at

$$\sin \phi_{\text{EGL}} = \frac{1}{\sin \theta} \left[ \frac{m}{|m|} \sqrt{1 - \left(\cos \theta + n \frac{\lambda}{2d}\right)^2 - m \frac{\lambda}{b}} \right]$$

$$(m = 0, \pm 1, ...), (n = 0, \pm 1, ...)$$
(38)

where (m + n) is even. <sup>7</sup>

<sup>9.</sup> Herper, J.C., Esposito, F.J., Rothenberg, C., and Hessel, A. (1977) Surface resonances in a radome covered dipole array, IEEE Antennas Propag. Symp. Dig., Stanford University, Stanford, Calif., 198-201.

Figure 21 shows the local grating lobe diagram for the grid of type (a). It is seen that, in this case, relevant grating lobes are (-1, -1) and (0, -2). According to Eq. (38), an off H-plane grating lobe (-1, -1) should cause narrowing of the element pattern with decreasing  $\theta$ . This is in contrast to the rectangular grid reference array case where the EGL effect is due to an H-plane (-1, 0) grating lobe. As a result, the rectangular grid element pattern widens with  $\theta$  tending toward the axis [see Figure 9 and Eq. (36)]. Based on Eq. (38), one expects for  $b/\lambda = 0.6$ ,  $d/\lambda = 0.7$  that  $\phi_{\rm EGL} = 75^{\circ}$  for  $\theta = 90^{\circ}$  and  $\phi_{\rm EGL} = 51^{\circ}$  for  $\theta = 70^{\circ}$ . The smooth pattern in the H-plane and narrowing of the patterns (with decreasing  $\theta$ ) as well as the predicted values of  $\phi_{\rm EGL}$  are also observed in Figure 21. In addition, one finds an increased sharpness of the EGL drop-off and an increased level of the associated off-broadside ripple with decreasing  $\theta$ . Such behavior is not unexpected because of the increase of mutual coupling when the grating lobe propagation direction approaches the principal H-plane with decreasing  $\theta$ .

As expected, the E-plane element gain performance is found to be similar in both the triangular and the rectangular lattice arrays, since, in both cases, the axial grating lobe is located at  $-\lambda/d$ .

The alternative grid (b) and the pertinent grating lobe diagram are shown in Figure 22. The  $\theta$  = 90° pattern is similar to that for the rectangular grid reference array, which is plausible because of the same grating lobe location. In the range  $\theta$  = 65° to 90°, the influence of the grating lobe (-2, 0) on the element pattern is dominant. According to Eq. (38), however, at  $\theta$  = 60°, two EGL effects are expected: one for  $\phi_{\rm EGL}$  = 67° due to the scanned off H-plane grating lobe (-2, 0); the other at  $\phi_{\rm EGL}$  = 32° due to the off-principal-plane grating lobe (-1, -1). Both are barely noticeable in Figure 22. As  $\theta$  decreases, the former grating lobe moves toward larger values of  $\phi$ , while the latter approaches  $\phi$  = 0°. For  $\theta$  = 50°, the dip is predicted to appear at  $\phi_{\rm EGL}$  = 16° and, for  $\theta$  = 40°, at 0.7°, which is well borne out in Figure 22. For a further decrease in  $\theta$ , in addition to (-1, -1), the (1, -1) grating lobe also moves into real space, both at  $\phi$  = 0°. This results in a sharp E-plane dip shown for  $\theta$  = 30°. With increasing values of  $\phi$  (for  $\theta$  = 30°), the (1, -1) grating lobe moves out of real space, which produces the peak in the element pattern gain near  $\phi$  = 20° in Figure 22.

The E-plane gain roll-off is slower than in the rectangular grid reference array case, because the E-plane grating lobe is further removed from the real space edge.

In view of the above data, the choice of rectangular versus triangular grid is based on the maximum axial scan-angle, the extent of the excited array arc, and the desired frequency bandwidth. As the numerical results show, the lattice design of large, cylindrical, uniformly spaced arrays may be safely based on the lo-

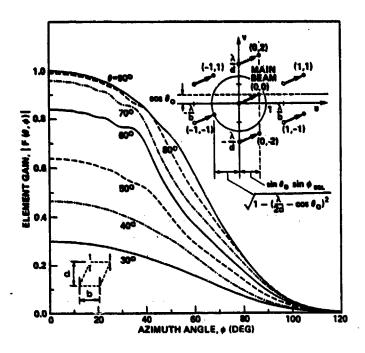


Figure 21. Voltage Element Gain Pattern and Corresponding Local Grating Lobe Diagram [Triangular Grid (a)  $b/\lambda = 0.6$ ,  $d/\lambda = 0.7$ , ka = 120]. Parameter: elevation angle  $\theta = 30^{\circ}$ ,  $40^{\circ}$ ,...,  $90^{\circ}$ 

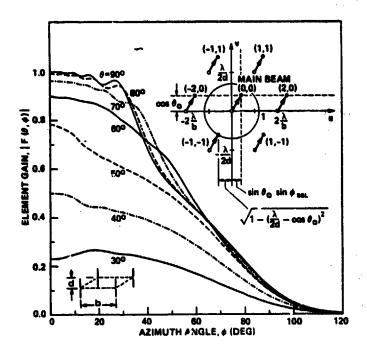


Figure 22. Voltage Element Gain Pattern and Corresponding Local Grating Lobe Diagram [Triangular Grid (b)  $b/\lambda = 1.2$ ,  $d/\lambda = 0.35$ , ka = 120]. Parameter: elevation angle  $\theta = 30^{\circ}$ ,  $40^{\circ}$ , ...,  $90^{\circ}$ 

cal grating lobe diagram. (This, of course, excludes any blind spots due to feed effects.)

## 5.3 Comparison With Other Results

The few relevant references found in the literature are as follows:

- 1. An asymptotic Green's function in the presence of a conducting cylinder is employed to analyze circular arrays of axial dipoles in a rectangular lattice. Comparison of numerical results with those based on modal analysis leads to the conclusion that, although qualitative element pattern features in the forward region such as the EGL drop-off and the off-broadside ripple are exhibited, the details differ from those obtained from modal analysis in the following: (1) The  $\theta$  = 75° near  $\phi$  = 0° average level is higher than that in the principal H-plane, which is at variance with the present results and with those for planar arrays; (2) The E-plane element gain loss at  $\theta$  = 60° (off axis) is about 25 percent, as compared with the 32 percent roll-off predicted by modal analysis; (3) No shadow region results are presented; (4) The matching scheme and the pattern normalization are unclear and no absolute element gain information is presented.
- 2. Another result is found. Here, the analysis was carried out by an interesting boundary layer method, using the parabolic equation approximation applied to uniformly spaced arrays on convex cylindrical surfaces of arbitrary but slowly varying curvature. The results relevant to this report are contained in Figure 3 of Indenbom and Filippov for  $b/\lambda = 0.6$  and  $d/\lambda = 0.54$ . For convenience, this figure is reproduced in Figure 23 here along with results for  $\theta = 60^{\circ}$  and 90° obtained by modal analysis. The normalized voltage element gain pattern in the  $\theta = 90^{\circ}$  cut compares well with that based on modal analysis. However, the pattern for  $\theta = 60^{\circ}$  does not match our results, both in the  $\phi = 0^{\circ}$  gain level and in the element pattern shape. It exhibits two types of ripples absent in our results and not accompanied by the usual EGL dips. From the grating lobe structure for the geometry in question, EGL effects are predicted in this case, and, therefore, the pattern is expected to be smooth.
- 3. We have also compared our results with results for cylindrical arrays of aperture elements. The mutual coupling effects, such as the endfire grating lobe condition gain drop-off and the off-broadside ripple in dipole arrays above cylindrical ground are found to be considerably weaker than in similar arrays of aper-

ture elements, in various analyses. <sup>1, 4, 10, 11, 13</sup> This is expected, in view of the appearance of dipole "images" with phase reversed currents that tend to reduce the mutual coupling in dipole arrays. By contrast, in aperture arrays, the "images" reinforce the excitation of mutual coupling effects. It is reasonable to compare the element patterns for arrays of axial dipoles with those of circumferentially polarized rectangular waveguide elements, since, in both cases, the circumferential plane corresponds to the direction of the strongest mutual coupling. It can be seen from Sureau and Hessel <sup>10</sup> and Figure 24 that, in the case of rectangular aperture elements, the EGL effect appears as a pronounced dip and not merely as pattern drop-off. Also, the off-broadside ripple level is appreciably higher than in dipole arrays.

#### 6. CONCLUSION

The numerical results for the element pattern of an axial dipole element in a cylindrical phased array lead to the following conclusions:

- 1. The grating lobe effects on the element gain and phase pattern in uniformly spaced, large radius, circular cylindrical arrays of axial dipoles are reliably predicted by locally planar-grating lobe diagrams for either rectangular or triangular lattices.
- 2. The creeping waves interfere with the direct element radiation in the forward region and produce a far field in the shadow region with an angular attenuation constant proportional to  $(ka \sin \theta)^{1/3}$ . The influence of both effects on the element pattern (ripples in the forward region and finite values of the pattern in the shadow region) must be known to predict the sidelobe performance of cylindrical phased arrays accurately.
  - 3. For a given lattice and frequency, the element gain pattern is insensitive

<sup>10.</sup> Sureau, J.C., and Hessel, A. (1972) Realized gain function for a cylindrical array of open-ended waveguides, in Phased Array Antennas, A.A. Oliner and G.H. Knittel, Eds., Artech House, Dedham, Mass.

<sup>11.</sup> Borgiotti, G.V., and Balzano, Q. (1970) Mutual coupling analysis of a conformal array of elements on a cylindrical surface, IEEE Trans. Antennas Propag., AP-18(No. 1).

<sup>12.</sup> Borgiotti, G. V., and Balzano, Q. (1972) Analysis and element pattern design of periodic arrays of circular apertures on conducting cylinders, <u>IEEE Trans. Antennas Propag.</u>, AP-20(No. 5).

<sup>13.</sup> Borgiotti, G.V., and Balzano, Q. (1972) Conformal arrays on surfaces with rotational symmetry, in <u>Phased Array Antennas</u>, A.A. Oliner and G.H. Knittel, Eds., Artech House, Dedham, Mass.

<sup>14.</sup> Collin, R.E. (1960) Field Theory of Guided Waves. McGraw-Hill.

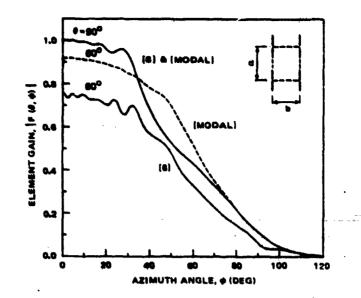


Figure 23. Comparison of Voltage Element Gain Patterns Between Figure 36 and Results Based on Modal Analysis (b/ $\lambda$  = 0.6, d/ $\lambda$  = 0.54, L/ $\lambda$  = 0.5, s/ $\lambda$  = 0.25, w/ $\lambda$  = 0.05, h/ $\lambda$  = 0.01, ka = 125.7). Parameter: elevation angle  $\theta$  = 60°, 90°

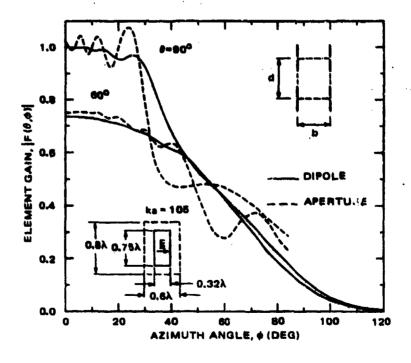


Figure 24. Comparison of Voltage Element Gain Patterns Between Dipole and Rectangular Aperture Radiators,  $^{11}$  (b/ $\lambda$  = 0.6, d/ $\lambda$  = 0.8, ka = 105)

to the element dimensions and ground plane spacing, provided in each case that the element is appropriately "broadside" matched.

- 4. The anmatched gap impedance exhibits significant dependence on dipole length and its distance to ground. Thus, the basic limitations of the dipole element rests in its scan and frequency-dependent impedance properties and those of the matching scheme.
- 5. The gap impedance is similar to that of a corresponding planar array. Therefore, planar array simulator techniques for designing and matching radiating elements can be used.
- 6. The dipole phase center is located near the element and not on the grounding surface.
- 7. Mutual coupling effects, except for possible E-plane feed interactions producing blind spots, are less pronounced than in similar aperture arrays.
- 8. Polarization purity, wide bandwidth, lower mutual coupling effects, ease of fabrication, and low cost make the axial dipole a suitable element for cylindrical phased arrays.
- 9. The theoretical results compare well with experiment (see Part 2 of this report).

# References

- Hessel, A. (1972) Mutual coupling effects in circular arrays on cylindrical surfaces-Aperture design implications and analysis, in <u>Phased Array Antennas</u>, A.A. Oliner and G.H. Knittel, Eds., Artech House, Dedham, Mass.
- 2. Mailloux, R.J. (1982) Phased array theory and technology, <u>Proc. IEEE</u>, 70(No. 3).
- 3. Herper, J.C., Hessel, A., Mandarino, C., and Tomasic, B. (1980) Performance of a dipole element in a cylindrical array A modal approach, IEEE Antennas Propag. Symp. Dig., University of Laval, PQ, Canada, 162-165.
- 4. Sureau, J.C., and Hessel, A. (1971) Element pattern for circular arrays of waveguide-fed axial slits on large conducting cylinders, <u>IEEE Trans. Antennas Propag.</u>, AP-19, 64-76.
- 5. Eichmann G., and Lee, K.S. (1978) Analysis of conformal scanning dipole arrays, ...intennas Propag. Symp. Dig., University of Maryland, Washington, D.C.
- 6. Indenbom, M.V., and Filippov, V.S. (1978) An asymptotic solution of the problem of mutual coupling between the radiators of a convex cylindrical array antenna, Radio Eng. Electron Phys., 23(No. 1), 42-49.
- 7. Abramowitz, M., and Stegun, I. (1964) <u>Handbook of Mathematical Functions</u>, U.S. Dept. Commerce, Nat. Bur. Stand.
- 8. Lee, S.W., Jones, W.R., and Campbell, J.J. (1970) Convergence of numerical solution of iris-type discontinuity problems, Antennas Propag. Symp. Dig., Ohio Stail liversity, Columbus.
- 9. Herper, J.C., Esposito, F.J., Rothenberg, C., and Hessel, A. (1977) Surface resonances in a radome covered dipole array, IEEE Antennas Propag. Symp. Dig., Stanford University, Stanford, Calif., 198-201.
- 10. Sureau, J.C., and Hessel, A. (1972) Realized gain function for a cylindrical array of open-en waveguides, in Phased Array Antennas, A.A. Oliner and G.H. Knitte's., Artech House, Dedham, Mass.

- 11. Borgiotti, G.V., and Balsano, Q. (1970) Mutual coupling analysis of a conformal array of elements on a cylindrical surface, IEEE Trans. Antennas Propag., AP-18(No. 1).
- 12. Borgiotti, G.V., and Balzano, Q. (1972) Analysis and element pattern design of periodic arrays of circular apertures on conducting cylinders, IEEE Trans. Antennas Propag., AP-20(No. 5).
- 13. Borgiotti, G.V., and Balsano. Q. (1972) Conformal arrays on surfaces with rotational symmetry, in <u>Phased Array Antennas</u>, A.A. Oliner and G.H. Knittel, Eds., Artech House, Dedham, Mass.
- 14. Collin, R.E. (1960) Field Theory of Guided Waves, McGraw-Hill.

#### Appendix A

# Floquet's Theorem for Isosceles Triangular Array Lattice

With reference to Figure 4, let the usual Floquet expansion for any field component in the unit cell of size  $(2\pi/N \times 2d)$  be

$$\Psi = \sum_{m,n=-\infty}^{\infty} \mathbf{a}_{mn}(\rho) e^{-\mathbf{j}(\nu_m \phi + \mathbf{k}_{zn} \mathbf{z})}$$
(A1a)

where amn are the amplitude coefficients of the (m,n)th Floquet mode, with

$$\nu_{\rm m} = \nu + {\rm mN} = \nu + \frac{2\pi}{\alpha} {\rm m}$$
 (M = 0, ±1,...) (A1b)

and

$$k_{zn} = k_{zo} + \frac{\pi}{d} n$$
 (A1c)

For a triangular lattice, Floquet's theorem imposes an additional constraint on Eq. (A1a) so that a displacement by  $(\pi/N)$  in  $\phi$  followed by that of d in z multiplies the field by the phase constant  $\exp(-j\delta)$ , that is,

$$\Psi \left( \phi + \frac{\pi}{N} , z + d \right) = e^{-j\delta} \Psi \left( \phi, z \right)$$
 (A2)

It is seen from Figure A1 that

$$\delta = \nu \frac{\pi}{N} + k_{20}d. \tag{A3}$$

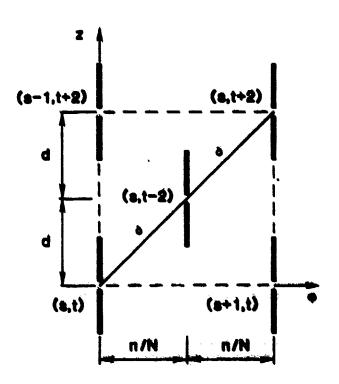


Figure A1. Unit Cell Cross Section at  $\rho = \rho_0$  of a Circular Cylindrical Array With Triangular Lattice

Substituting Eqs. (A1a) and (A3) into Eq. (A2), one finds

$$\sum_{m,n=-\infty}^{\infty} a_{mn} \quad e^{-j} \left( \nu_m \phi^{+} k_{2n} z \right) \quad e^{-j} \left( \nu_m \frac{\pi}{N} + k_{2n} d \right)$$

$$= e^{-j(\nu_{N}^{\frac{m}{2}} + k_{zo}d)} \sum_{m = -\infty}^{\infty} a_{mn} e^{-j(\nu_{m}\phi + k_{zn}z)}.$$
 (A4)

Using Eqs. (A1b) and (A1c) and the orthogonality of the Floquet basis in Eq. (A1a),

$$-j(\nu_{m} + k_{zn} d) = -j(\nu_{N} + k_{zo} d) -j(m\pi + n\pi)$$
 (A5)

whereupon, it follows that

$$a_{mn} [e^{-j(m+n)\pi} -1] = 0.$$
 (A6)

Thus,  $a_{mn} = 0$  unless (m + n) is an even integer. Consequently, we conclude that in an isosceles triangular lattice, Floquet modes with (m + n) odd are not excited.

# Appendix B

# Single Element Excitation in a Triangular Lattice

A single (s = 0, t = 0) element excitation in the triangular isosceles lattice of Figure 4 is expressed in terms of an excitation vector  $\underline{\mathbf{a}} = \{\delta_{s0} \delta_{t0}\}$  (s = 0, 1,..., N - 1; t = 0, $\pm$ 1,...) where

$$\delta_{so} \delta_{to} = \frac{d}{4\pi N} \sum_{\nu=-N}^{N-1} e^{-j\nu(\frac{2\pi}{N}s + \frac{\pi}{N}t)} \int_{-\pi/d}^{\pi/d} e^{-jk_{so}dt} dk_{so}.$$
 (B1)

Each exponential term in Eq. (B1) represents a unity-amplitude progressively-phased array excitation  $2\pi\nu/N$  in the angular direction and  $k_{\rm go}d + \pi\nu/N$  in the skew direction. In this Appendix, we verify the identity Eq. (B1). To this end, one observes that

$$-\frac{d}{2\pi} \int_{-\pi/d}^{\pi/d} e^{-jk_{zo}dt} dk_{zo} = \delta_{to} \qquad (t=0,\pm 1,...).$$
 (B2a)

and

$$\frac{1}{2N}\sum_{\mu=N}^{N-1}e^{-j\nu\left(\frac{2\pi}{N}a+\frac{\pi}{N}t\right)}=\frac{1}{2N}\sum_{\nu=0}^{N-1}\left[e^{-j\nu\frac{\pi}{N}(2a+t)}+e^{j\left(\nu+1\right)\frac{\pi}{N}(2a+t)}\right]$$

$$=\frac{1}{N}\frac{\sin\pi(2s+t)}{1-e^{-j\frac{\pi}{N}(2s+t)}}=\delta_{2s+1,\;2(N)},\quad (\ell=0,\pm1,...).$$
(B2b)

The product of the left-hand sides of Eqs. (B2a) and (B2b) is

$$\delta_{to} \delta_{2s+t, 2\ell_n} = \delta_{to} \delta_{s, \ell_n}. \tag{B3}$$

Since s = 0, 1,..., N - 1, it follows that, in Eq. (B3), only the A=0 term contributes. Therefore,  $\delta_{to}$   $\delta_{2s+t}$ ,  $2\delta N$  =  $\delta_{to}$   $\delta_{so}$  Q.E.D.

## Appendix C

### Covergence Acceleration

As already mentioned in Section 4, the double sum in Eq. (16b) may be evaluated as  $\sum_{n=1}^{\infty} g_n \left(\sum_{m=1}^{\infty} f_{mn}\right)$ . In this Appendix, we describe a convergence acceleration of the series  $\sum_{m=1}^{\infty} f_{mn}$ . To this end, we write

$$\sigma_{n} = \sigma = \sum_{m=-\infty}^{\infty} f_{mn}$$
 (C1a)

where f<sub>mn</sub> is given by Eq. (16b) as

$$f_{mn} = \frac{\sin^2(\nu_m x)}{(\nu_m x)^2} \quad Z_{\nu_m}(\kappa_n; a, \rho) \quad H_{\nu_m}^{(2)}(\kappa_n \rho_0) \qquad \qquad (m = 0, \pm 1, ...)$$
(C1b)

with x =  $w/2\rho_0$ . For convenience, let  $\sigma = \sigma_0 + \sigma'$ , where  $\sigma_0 = f_{on}$  and

$$\sigma' = \sum_{m=-\infty}^{\infty} f_{mn} . \tag{C2}$$

The prime indicates the exclusion of the m = 0 term in the infinite sum. The method to be described is carried out for both the rectangular and the triangular lattice geometries.

#### C1. RECTANGULAR LATTICE

To facilitate convergence acceleration of  $\sigma$ , it is desirable to introduce the first-order large index asymptotic expression for  $Z_{\nu_m}H_{\nu_m}^{(2)}$ , that is,

$$Z_{\nu_{\mathbf{m}}}(\kappa_{\mathbf{n}}; \mathbf{a}, \rho) H_{\nu_{\mathbf{m}}}^{(2)}(\kappa_{\mathbf{n}}\rho_{\mathbf{o}}) \simeq -j J_{\nu_{\mathbf{m}}}(\kappa_{\mathbf{n}}\rho_{\mathbf{o}}) Y_{\nu_{\mathbf{m}}}(\kappa_{\mathbf{n}}\rho_{\mathbf{o}}) \sim j \frac{1}{\pi |\mathbf{m}| \mathbf{N}}. \tag{C3}$$

In view of Eq. (C3), one can rewrite Eq. (C2) in the following form:

$$\sigma' = \sum_{m=-\infty}^{\infty} f_{mn} + S \tag{C4a}$$

where, since  $\nu_{\rm m} = \nu + {\rm mN}$ ,

$$F_{mn} \sim \frac{\sin^2(\nu_m x)}{(\nu_m x)^2} \left[ Z_{\nu_m} \left( \kappa_n ; a, \rho_o \right) \right] \frac{H_{\nu_m}^{(2)}}{(\kappa_n \rho_o)} \left[ \frac{1}{\pi |m|N} - i \frac{\nu^2 + 2\nu mN}{\pi |m|^3 N^3} \right] (C4b)$$

and

$$S = j \frac{1}{\pi N^3 x^2} \sum_{m=-\infty}^{\infty} \frac{\sin^2(\nu_m x)}{|m|^3}.$$
 (C4c)

One observes that the series in Eq. (C4b) now converges as  $1/m^2$ . The sum S in Eq. (C4c) may be evaluated with the aid of Collin, <sup>14</sup> p. 579. The result is the rapidly convergent series:

$$S = j \frac{1}{\pi N^3 x^2} [A (1 - \cos(2\nu x)) - B]$$
 (C5a)

where

$$A = \sum_{m=1,2,3,...} \frac{1}{m^3} = 1.20205690$$
 (C5b)

and

B = 
$$(Nx)^2 \cos(2\nu x)$$
 [2 in  $(2Nx) - 3 - \frac{(Nx)^2}{18} - \cdots$ ]. (C5c)

### C2. TRIANGULAR LATTICE

In view of Eq. (A6), we distinguish two cases: For nodd

$$\sigma = \sum_{n=...,-3,-1,}^{1,3,...} F_{mn} + S_{odd}$$
 (n = ±1, ±3,...). (C6)

The series

$$S_{\text{odd}} = j \frac{1}{\pi N^3 x^2} \sum_{m=\dots-3-1}^{1.3...} \frac{\sin^2(\nu_m x)}{|m|^3}$$
 (C7a)

may be cast into a rapidly convergent form (Collin, 14 p. 580)

$$S_{\text{odd}} = j \frac{1}{\pi N^3 x^2} [A_{\text{odd}} (1-\cos(2\nu x) - B_{\text{odd}})]$$
 (C7b)

where

$$A_{\text{odd}} = \sum_{m=1,3,...} \frac{1}{m^3} = 1.05179979$$
 (C7c)

and

$$B_{\text{odd}} = (Nx)^2 \cos(2\nu x) \left[ \ln(Nx) - \frac{3}{2} + \frac{(Nx)^2}{18} - \cdots \right].$$
 (C7d)

When n is even

$$\sigma = \sigma_0 + \sum_{m = \dots, -4, -2} F_{mn} + S_e$$
 (C8a)

where

$$S_e = S - S_{odd}$$
 (C8b)

Appendix D

**Matching Networks** 

The load impedance is connected to the output terminals of a two-port matching network characterized by its scattering matrix.

In Section D1, we first derive expressions for the reflection coefficient at the input to the matching network and for total voltage at the load.

Similarly, in Section D2, we derive expressions for the reflection coefficient at the input to the matching network and for voltage at the load (dipole gap-impedance) which is now connected to output terminals of a matching network via a transmission line.

In Sections D3 to D5, we determine the elements of a scattering matrix for three specific simple matching networks: series, parallel, and quarter-wave transformer.

# D1. LOAD IMPEDANCE CONNECTED TO OUTPUT TERMINALS OF TWO-PORT MATCHING NETWORKS

The S-parameters of a linear, passive two-port network can be defined with the help of Figure D1. As shown in the figure,  $V_j^+$  (j=1,2) are the traveling waves incident on the junction, and  $V_j^-$  are the reflected traveling waves from the junction. By linearity, the incident and reflected waves are related by

$$V_{i}^{-} = \sum_{j=1}^{2} S_{ij} V_{j}^{+} \text{ for } i = 1, 2$$
 (D1a)

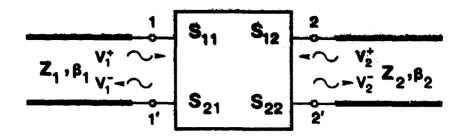


Figure D1. S-Parameter Representation of a Two-Port Network

or

$$V_1^- = S_{11} V_1^+ + S_{12} V_2^+$$
 (D1b)

$$V_2^- = S_{21} V_1^+ + S_{22} V_2^+$$
 (D1e)

From Eq. (D1b), it is seen that  $S_{11}$  is the reflection coefficient in the input guide 1, with guide 2 terminated in a matched load. Also,  $S_{21}$  is the transmission coefficient into guide 2 from guide 1 under the same condition. Similar statements apply to the parameters  $S_{22}$  and  $S_{12}$ .

If guide 2, with its characteristic impedance  $Z_2$ , is terminated by an impedance  $Z_{22}$ , at the terminal plane (2-2') (see Figure D2), then  $V_2$  may be regarded as the incident wave on  $Z_{22}$ , and  $V_2^+$  is the wave reflected from  $Z_{22}$ . The ratio must be equal to the reflection coefficient of the load; hence,

$$\Gamma_2 = \frac{V_2^+}{V_2^-} = \frac{Z_{22} - Z_2}{Z_{22} + Z_2} . \tag{D2}$$

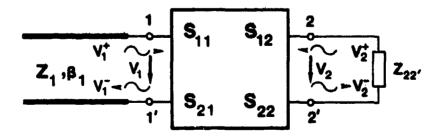


Figure D2. Two-Port Matching Network Connecting Load Impedance Z<sub>22</sub>- With Transmission Line 1

Using Eqs. (D1) and (D2), one can now determine the input reflection coefficient  $\Gamma_1$  in terms of S parameters and  $\Gamma_2$ :

$$V_1^- = S_{11} V_1^+ = S_{12} V_2^+ = S_{12} \Gamma_2 V_2^-$$
 (D3a)

$$S_{12} V_1^+ = V_2^- - S_{22} \Gamma_2 V_2^-$$
 (D3b)

so that

$$\Gamma_1 = \frac{V_1^-}{V_1^+} = S_{11} - \frac{S_{12} S_{21} \Gamma_2}{S_{22} \Gamma_2 - 1} = \frac{S_{11} - \Delta \Gamma_2}{1 - S_{22} \Gamma_2}$$
(D3e)

with

$$\Delta = S_{11} S_{22} - S_{12} S_{21}. \tag{D3d}$$

Consequently, the input impedance is

$$Z_{\rm in} = Z_1 \frac{1 + \Gamma_1}{1 - \Gamma_1}$$
 (D4)

One can also find total voltage  $\mathbf{V_2}$  at the load in terms of the S parameters and the incident voltage  $\mathbf{V_1^+}$ :

In view of Eq. (D2), one has

$$V_{2}^{-} = S_{21} V_{1}^{+} + S_{22} \Gamma_{2} V_{2}^{-}$$
 (D5a)

or

$$V_2^- = \frac{S_{21}}{1 - S_{22} \Gamma_2} V_1^+. \tag{D5b}$$

Using

$$\mathbf{V_1^-} = \Gamma_1 \mathbf{V_1^+} \tag{D6a}$$

one finds from Eq. (D1b)

$$v_{2}^{+} = \frac{\overline{v_{1}} - s_{11} \ v_{1}^{+}}{s_{12}} = \frac{\Gamma_{1} \ v_{1}^{+} - s_{11} \ v_{1}^{+}}{s_{12}} = \frac{\Gamma_{1} - s_{11}}{s_{12}} \ v_{1}^{+}$$
 (D6b)

or, upon substitution of  $(\Gamma_1 - S_{11})$ , from Eq. (D3c)

$$V_2^+ = -\frac{S_{21} \Gamma_{22}}{S_{22} \Gamma_{22} - 1} V_1^+ . \tag{D6c}$$

Using Eqs. (D5b) and (D6c), the total voltage at (2 - 2') is

$$V_2 = V_2^+ + V_2^- = \frac{S_{21} (1 + \Gamma_2)}{1 - S_{22} \Gamma_2} V_1^+.$$
 (D7)

When the input line is matched as shown in Figure D3, one readily sees that

$$V_2 = V_2^+ + V_2^- = V_2^+ (1 + S_{22}^-)$$
 (D8m)

or

$$V_2^+ = \frac{V_2}{1 + S_{22}}$$
 (D8b)

and, consequently, since  $V_{1}^{+} = 0$ ,

$$V_1 = V_1 - S_{12} V_2 - \frac{S_{12}}{1 + S_{22}} V_2.$$
 (D8c)

The output impedance is then

$$Z_{\text{out}} = Z_2 \frac{1 + S_{22}}{1 - S_{22}}$$
 (D9)

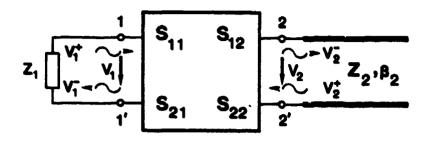


Figure D3. Two-Port Network Connecting Matched-Transmission Line 1 With Transmission Line 2

# D2 LOAD (DIPOLE GAP IMPEDANCE) CONNECTED TO OUTPUT TERMINALS OF TWO-PORT NETWORK VIA TRANSMISSION LINE

Transmission line of length  $L_2$  is terminated with dipole gap (load) impedance  $Z_g$  and connected to output terminals of matching network as shown in Figure D4. The output transmission line 2 has characteristic impedance  $Z_2$  and propagation constant  $\beta_2$ .

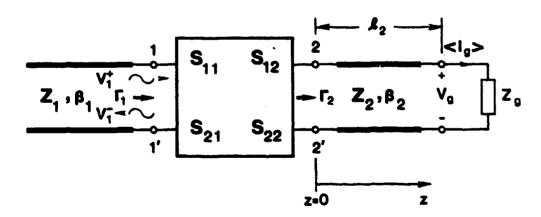


Figure D4. Load Impedance  $Z_g$  Connected to Matching Network via Transmission Line

In this case, from Eq. (D3c), the reflection coefficient at the input to the matching network is

$$\Gamma_1 = \frac{S_{11} - 4\Gamma_2}{1 - S_{22} \Gamma_2}$$
 (D10a)

where now

$$\Gamma_2 = \Gamma_g e^{-j2\beta_2 L_2} \tag{D10b}$$

and

$$\Gamma_{\rm g} = \frac{Z_{\rm g} - Z_{\rm 2}}{Z_{\rm g} + Z_{\rm 2}}$$
 (D10c)

To find total voltage at  $z = A_{2}$ , that is,  $V_g = V(z = A_2)$ , in terms of incidence voltage  $V_1^+$  at the input port  $(1 - 1^-)$  of the matching network, it is convenient to proceed as follows:

$$V_2(z=0^+)=V_2^+(z=0^+)+V_2^-(z=0^+)=V_2^+(z=0^+)(1+\Gamma_2)$$
 (D11a)

where

$$\Gamma_2 = \frac{V_2^- (z=0^+)}{V_2^+ (z=0^+)} = \Gamma_g e^{-j2\beta_2 L_2}$$
 (D11b)

and  $\Gamma_{\mathbf{g}}$  is given by Eq. (D10c). Using relations

$$V_2(z) = V_2^+ (z = 0^+) e^{-j\beta_2 z} + V_2^- (z = 0^+) e^{j\beta_2 z}$$

$$= V_2^+ (z = 0^+) e^{-j\beta_2 z} (1 + \Gamma_2 e^{j2\beta_2 z})$$
 (D12a)

and Eq. (D11b), total voltage at the load is

$$V_2 (z = I_2) = V_g = V_2^+ (z = 0^+) e^{-j\beta_2 I_2} (1 + \Gamma_g).$$
 (D12b)

Substitution of Eq. (D12a) into Eq. (D12b) yields

$$V_g = V (z = 0^+) e^{-j\beta_2 L_2} \frac{1 + \Gamma_g}{1 + \Gamma_2}$$
 (D13)

Furthermore, substituting Eq. (D7) into Eq. (D13), we finally obtain

$$V_{g} = \frac{S_{21} (1 + \Gamma_{g})}{1 - S_{22} \Gamma_{2}} e^{-j\beta_{2} A_{2}} V_{1}^{+}.$$
 (D14)

# D3. S-PARAMETERS OF THE SERIES MATCHING NETWORK

The scattering-matrix elements will be evaluated for the series-matching network connecting two lines with characteristic impedances  $Z_1$  and  $Z_2$  as shown in Figure D5. This matching network, which consists of transformer and series reactance in cascade connection, is employed in Section D5 for matching the dipole gap impedance  $Z_g(\nu, \mathbf{k}_{\geq 0})$  to TEM feed-transmission line.

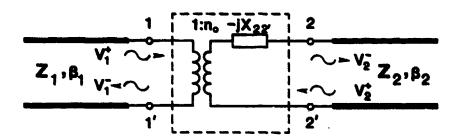


Figure D5. Series Matching Network

The values of the transformer ratio  $n_0$  and the reactance  $X_{22}$  ( $\nu$ ,  $k_{z0}$ ) are chosen so that active reflection coefficient  $\Gamma_1(\nu, k_{z0})$  at the input side of the matching network is zero. To determine  $n_0$  and  $X_{22}$  ( $\nu$ ,  $k_{z0}$ ), we first write the expression for impedance at the output terminals (2 - 2°) of the matching network. In reference to Figure D4, the impedance looking into transmission line 2 at z = 0 is

$$Z_{22}(\nu, k_{z0}) = R_{22}(\nu, k_{z0}) + j X_{22}(\nu, k_{z0})$$

$$= Z_{2} \frac{Z_{g}(\nu, k_{z0}) \cos \beta_{2} A_{2} + j Z_{2} \sin \beta_{2} A_{2}}{Z_{2} \cos \beta_{2} A_{2} + j Z_{g}(\nu, k_{z0}) \sin \beta_{2} A_{2}}$$
(D15a)

where the gap impedance

$$Z_g(\nu, k_{z_0}) = R_g(\nu, k_{z_0}) + j X_g(\nu, k_{z_0}).$$
 (D15b)

Thus.

$$n_0 = \sqrt{\frac{R_{22} \cdot (\nu, k_{EQ})}{Z_1}} . \tag{D16}$$

With elements of the series matching network so defined, the corresponding S-parameters can be found as follows:

If the output line is matched as shown in Figure D6, we have

$$S_{11} = \frac{V_{1}^{-}}{V_{1}^{+}} \Big|_{V_{2}^{+}=0} = \frac{Z_{1n} - Z_{1}}{Z_{1n} + Z_{1}} = \frac{\frac{Z_{2} - j X_{22} \cdot (\nu, k_{z0})}{z_{2} - j X_{22} \cdot (\nu, k_{z0})} - Z_{1}}{\frac{Z_{2} - j X_{22} \cdot (\nu, k_{z0})}{z_{0}^{2}} + Z_{1}}$$

$$= \frac{Z_{2} - Z_{22} \cdot (\nu, k_{z0})}{Z_{2} + Z_{22}^{*} \cdot (\nu, k_{z0})}$$
(D17)

where  $Z_{22}$  ( $\nu$ ,  $k_{z0}$ ) is given by Eq. (D15a).

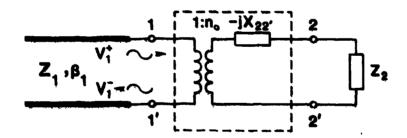


Figure D6. Network Illustrating Evaluation of  $S_{11}$  and  $S_{21}$  of Series Matching Network

With the input line matched (see Figure D7), one has

$$S_{22} = \frac{V_2^-}{V_1^+} \Big|_{V_1^+=0} = \frac{Z_{\text{out}} - Z_2}{Z_{\text{out}} + Z_2} = \frac{Z_1 n_0^2 - j X_{22} \cdot (\nu, k_{z0}) - Z_2}{Z_1 n_0^2 - j X_{22} \cdot (\nu, k_{z0}) + Z_2}$$

$$= \frac{Z_{22}^+ \cdot (\nu, k_{z0}) - Z_2}{Z_2 + Z_{22}^+ \cdot (\nu, k_{z0})}.$$
(D18)

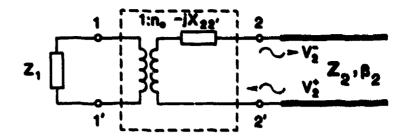


Figure D7. Network Illustrating Evaluation of S22 and  $\rm S_{12}$  of Series Matching Network

To find  $S_{21}$ , we again consider the output line matched (see Figure D6). On the input line, we have

$$V_1 = V_1^+ + V_1^- = V_1^+ (1 + S_{11})$$
 (D19a)

and

$$I_1 = Y_1 (V_1^+ - V_1^-) = Y_1 V_1^+ (1 - S_{11}^-)$$
 (D19b)

Since

$$-I_2 = I_2^2 = \frac{I_1}{n_0} = \frac{Y_1 V_1^+}{n_0} (1 - S_{11})$$
 (D20a)

and

$$I_2^- = Y_2 V_2^-$$
 (D20b)

we see that

$$Y_2 V_2 = \frac{Y_1 V_1^{\dagger}}{n_0} (1 - S_{11}).$$
 (D20c)

We now obtain

$$S_{21} = \frac{V_2^-}{V_1^+} \bigg|_{V_2^+=0} = \frac{Y_1}{Y_2 n_0} (1 - S_{11}) = \frac{2n_0 Z_2}{Z_2 + n_0^2 Z_1 - j X_{22} \cdot (\nu, k_{z0})}$$
$$= \frac{Z_2}{Z_1} \frac{2 \sqrt{R_{22} \cdot (\nu, k_{z0}) Z_1}}{Z_2 + Z_{22}^* \cdot (\nu, k_{z0})}. \tag{D21}$$

Similarly, with the aid of Figure D7, one can determine  $S_{12}$ , that is,

$$I_2 = \frac{I_1^-}{n_0} = Y_2 (V_2^+ - V_2^-) = Y_2 V_2^+ (1 - \frac{V_2^-}{V_2^+}) = Y_2 V_2^+ (1 - S_{22}^-)$$
 (D22a)

$$V_1 = I_1 Z_1 = n_0 I_2 Z_1 = \frac{Z_1}{Z_2} n_0 V_2^+ (1 - S_{22})$$
 (D22b)

so that

$$S_{12} = \frac{V_1^-}{V_2^+} \Big|_{V_1^+=0} = \frac{Z_1}{Z_2} n_0 (1 - S_{22}) = \frac{3n_0 Z_1}{Z_2 + Z_1 n_0^2 - j X_{22} \cdot (\nu, k_{20})}$$

$$= \frac{2 \sqrt{R_{22} \cdot (\nu, k_{20}) Z_1}}{Z_2 + Z_{22} \cdot (\nu, k_{20})}.$$
(D23c)

Notice the reciprocity relationship

$$Z_2S_{12} = Z_1S_{21}$$
 (D23)

#### D4. S-PARAMETERS OF A PARALLEL MATCHING NETWORK

Here, we evaluate a scattering matrix of a parallel two port matching network which consists of the transformer and susceptance in cascade connection, as shown in Figure D8.

The values of the transformer ratio  $n_0$  and the susceptance  $B_{22}$ . (\*\*,  $k_{\pm 0}$ ) are

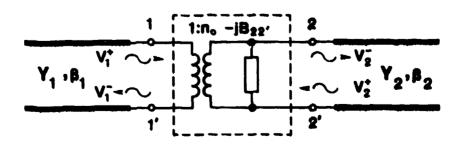


Figure D8. Parallel Matching Network

chosen so that the active reflection coefficient  $\Gamma_1$  ( $\nu$ ,  $k_{=0}$ ) at the input side of the matching network is zero for the specific set of  $\nu$ ,  $k_{=0}$  (see Figure D4). The transformer ratio  $n_0$  and susceptance  $B_{22}$  - ( $\nu$ ,  $k_{=0}$ ) can be determined from the relation for admittance at the output terminals of the matching network (2 - 2°) looking into transmission line 2, which is

$$Y_{22}(\nu, k_{z0}) = \frac{1}{Z_{22}(\nu, k_{z0})} = G_{22}(\nu, k_{z0}) + jB_{22}(\nu, k_{z0})$$
 (D24)

where  $Z_{22}$  - ( $\nu$ ,  $k_{20}$ ) is given by Eq. (D15a). It is seen that

$$n_0 = \sqrt{\frac{Y_1}{G_{22} \cdot (\nu, k_{m0})}}$$
 (D25)

Next, we determine the S-parameters of the parallel matching network. With the help of Figure D6, we write

$$S_{11} = \frac{V_{1}^{-}}{V_{1}^{+}} \Big|_{V_{2}^{+}=0} = \frac{Y_{1} - Y_{in}}{Y_{1} + Y_{in}} = \frac{Y_{1} - n_{0}^{2} (Y_{2} - jB_{22} - (\nu, k_{s0}))}{Y_{1} + n_{0}^{2} (Y_{2} - jB_{22} - (\nu, k_{s0}))}$$

$$= \frac{Y_{22} \cdot (\nu, k_{z0}) - Y_2}{Y_{22}^{*} \cdot (\nu, k_{z0}) + Y_2}$$
(D26a)

and

$$S_{21} = \frac{V_2^-}{V_1^+} \Big|_{V_2^+=0} = \frac{Y_1}{Y_2 n_0} (1 - S_{11}) = \frac{2Y_1}{n_0} \frac{1}{Y_{22}^+ - (\nu, k_{s0}) + Y_2}.$$
 (D26b)

With the aid of Figure D10, following a similar procedure, one determines  $\mathbf{S}_{22}$ , that is,

$$S_{22} = \frac{V_{2}^{-}}{V_{2}^{+}} = \frac{Y_{2} - Y_{\text{out}}}{Y_{2} + Y_{\text{out}}} = \frac{Y_{2} - \frac{Y_{1}}{n_{0}^{2}} + jB_{22} \cdot (\nu, k_{z0})}{Y_{2} + \frac{Y_{1}}{n_{0}^{2}} - jB_{22} \cdot (\nu, k_{z0})}$$

$$= \frac{Y_{2} - Y_{22}^{*} \cdot (\nu, k_{z0})}{Y_{2} + Y_{22}^{*} \cdot (\nu, k_{z0})}$$
(D27a)

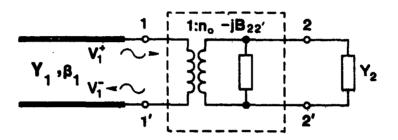


Figure D9. Network Illustrating Evaluation of  $S_{11}$  and  $S_{21}$  of the Parallel Matching Network

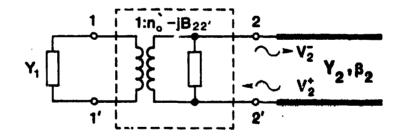


Figure D10. Network Illustrating Evaluation of  $S_{22}$  and  $S_{12}$  of the Parallel Matching Network

while  ${\rm S}_{12}$  can be determined from the same figure following the procedure indicated in the previous section or via a reciprocity relation, that is,

$$S_{12} = \frac{Y_2}{Y_1} S_{21} . ag{D27b}$$

# D5. S-PARAMETERS OF THE QUARTER-WAVELENGTH TRANSFORMER MATCHING NETWORK

A matching network, shown in Figure D11, consists of a transmission line with characteristic impedance  $Z_{\rm t}$  and propagation constant  $\beta_{\rm t}$ . The transmission line length is  $A_{\rm t} = \lambda_{\rm t}/4$ . The network is placed a distance  $A_{\rm 2}$  away from the dipole so that the transformed gap impedance  $Z_{\rm 22}$ , at terminals (2 - 2°) is real, that is,

$$Im [Z_{22}, (\nu, k_{20}, \lambda_2)] = 0$$
 (D28)

where  $Z_{22}$ ,  $(\nu, k_{z0}; L_2)$  is given by Eq. (D15a).

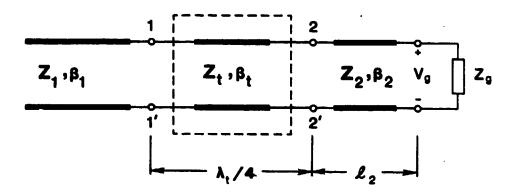


Figure D11. Quarter-Wave Transformer Matching Network

From Eq. (D28), we obtain the relation for  $L_2$ ,

$$tg 2\beta_2 I_2 = \frac{2Z_2 X_g (\nu, k_{z0})}{R_g^2 (\nu, k_{z0}) + Z_2^2 + X_g^2 (\nu, k_{z0})}$$
(D29a)

where gap impedance

$$Z_g(\nu, k_{z0}) = R_g(\nu, k_{z0}) + jX_g(\nu, k_{z0})$$
 (D29b)

and characteristic impedance of transmission line 2 is

$$Z_2 = R_g (\nu, k_{20})$$
 (D29c)

The characteristic impedance of  $\lambda_{+}/4$  transformer is then

$$Z_t = \sqrt{Z_1 \operatorname{Re}[Z_{22}/(\nu, k_{z0}; A_2)]}$$
 (D30a)

and the propagation constant

$$\beta_{t} A_{t} = \frac{\pi}{2} . \tag{D30b}$$

In the remaining part of this section, we determine the scattering parameters for a section of transmission line of length  $t_{t}$  and characteristic impedance  $Z_{t}$  shown in Figure D12.

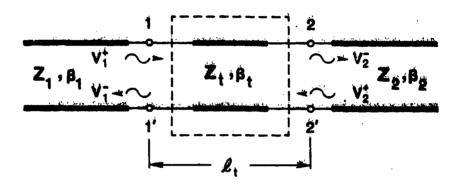


Figure D12. Quarter-Wavelength Transformer Matching Network Illustrating Evaluation of S-Parameters

Scattering parameters  $S_{\hat{1}\hat{1}}$  and  $S_{\hat{2}\hat{1}}$  are found with the help of Figure D13 as follows:

We define reflection coefficients

$$\Gamma(z = t_t) = \Gamma_2 = \frac{z_2 - z_t}{z_2 + z_t}$$
 (D31a)

and

$$\Gamma(z = 0^+) = \Gamma_2 e^{-j2\beta_t L_t}$$
 (D31b)

The impedance at the input port of the matching network is

$$Z(z=0) = Z_{t} \frac{1 + \Gamma(z=0^{+})}{1 - \Gamma(z=0^{+})}$$
 (D32)

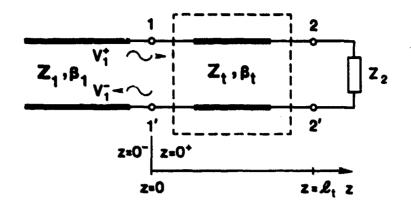


Figure D13. Network Illustrating Evaluation of S<sub>11</sub> and S<sub>21</sub> of Quarter-Wave Transformer Matching Network

Consequently, we may write

$$S_{11} = \frac{V_1^-}{V_1^+} \Big|_{V_2^+=0} = \frac{Z(z=0) - Z_1}{Z(z=0) + Z_1}.$$
 (D33)

Substituting Eq. (D31a) into Eq. (D31b), then Eq. (D31b) into Eq. (D32), and finally Eq. (D32) into Eq. (D33), we obtain

$$S_{11} = \frac{(Z_2 - Z_t)(Z_t + Z_1) e^{-j2\beta_t A_t} + (Z_t - Z_1)(Z_2 + Z_t)}{(Z_2 - Z_t)(Z_t - Z_1) e^{-j2\beta_t A_t} + (Z_t + Z_1)(Z_2 + Z_t)}.$$
(D34)

To find  $S_{21}$ , which is defined as

$$S_{21} = \frac{V_2^-}{V_1^+} \bigg|_{V_2^+=0}$$
 (D35a)

we first write the following relevant expression for the reflection coefficient at z = 0:

$$\Gamma(z = 0^{-}) = \Gamma_{1} = \frac{Z(z = 0) - Z_{1}}{Z(z = 0) + Z_{1}}$$
 (D35b)

For  $0 < z \leqslant \underline{s}_{t}$ , total voltage on the transmission line is

$$V(z) = V^{+}(0^{+}) e^{-j\beta_{t} z} \left(1 + \frac{V^{-}(0^{+})}{V^{+}(0^{+})} e^{j2\beta_{t} z}\right). \tag{D36}$$

At z = 1,,

$$V(A_t) = V^{+}(0^{+}) e^{-j\beta_t A_t} (1 + \Gamma(0^{+}) e^{-j2\beta_t A_t}).$$
 (D37)

Substituting Eq. (D31b) into Eq. (D37), we have

$$V(L_t) = V^+(0^+) e^{-j\beta_t L_t} (1 + \Gamma_2)$$
. (D38)

Furthermore, since

$$V(0^+) = V(0^-) = V(0)$$
 (D39a)

we see that

$$V(0^+) = V^+(0^+)(1 + \Gamma(0^+))$$
 (D39b)

and consequently, using Eqs. (D39a) and (D31b) from Eq. (D39b)

$$V^{+}(0^{+}) = \frac{V(0)}{1 + \Gamma(0^{+})} = \frac{V(0)}{1 + \Gamma_{2} - j2\beta_{1}A_{1}}.$$
 (D39c)

Here

$$V(0) = V(0^{-}) = V^{+}(0^{-}) (1 + \Gamma_{\tau})$$
 (D40a)

which, after substituting into Eq. (D39c), yields

$$V^{+}(0^{+}) = \frac{V^{+}(0^{-})(1 + \Gamma_{1})}{1 + \Gamma_{2} e^{-j2\beta_{1} \delta_{1}}}.$$
 (D40b)

Substituting Eq. (D40b) into Eq. (D38), we obtain

$$V(A_{t}) = \frac{V^{+}(0^{-}) (1 + \Gamma_{1}) e^{-j\beta_{t}A_{t}} (1 + \Gamma_{2})}{1 + \Gamma_{2} e^{-j2\beta_{t}A_{t}}}.$$
 (D41)

Using

$$V(A_t) = V^-(z = A_t^+)$$
 (D42a)

one can therefore write

$$S_{21} = \frac{V^{-}(z = A_{t}^{+})}{V^{+}(z = 0^{-})} = \frac{(1 + \Gamma_{1})(1 + \Gamma_{2})}{1 + \Gamma_{2} e^{-j2\beta_{t}L_{t}}} e^{-j\beta_{t}L_{t}}.$$
 (D42b)

Finally, substituting Eq. (D35b) for  $\Gamma_1$  into Eq. (D42b), we obtain

$$S_{21} = \frac{2Z_{t} (1 + \Gamma_{2})}{Z_{t} (1 + \Gamma_{2} e^{-j2\beta_{t}A_{t}}) + Z_{1} (1 - \Gamma_{2} e^{-j2\beta_{t}A_{t}})} e^{-j\beta_{t}A_{t}}$$
(D43)

where  $\Gamma_2$  is given by Eq. (D31a).

With the help of Figure D14, following the same procedure, one finds  $S_{22}$  and  $S_{12}$ . However, because of the symmetry of the matching network, one sees from Figures D13 and D14 that expressions for  $S_{22}$  can be deduced from Eq. (D34) by interchanging subscripts 1 and 2. Thus,

$$S_{22} = \frac{V_1^-}{V_2^+} = \frac{(Z_1 - Z_t)(Z_t + Z_2) e^{-j2\beta_t A_t} + (Z_t - Z_2)(Z_1 + Z_t)}{(Z_1 - Z_t)(Z_t - Z_2) e^{-j2\beta_t A_t} + (Z_t + Z_2)(Z_1 + Z_t)}.$$
 (D44)

Using a reciprocity relation, one can also write

$$S_{12} = \frac{Z_1}{Z_2} S_{21} \tag{D45}$$

where  $S_{21}$  is given by Eq. (D43).

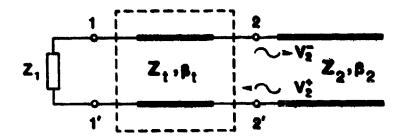


Figure D14. Network Illustrating Evaluation of S22 and S13 of Quarter-Wave Transformer Matching Network

Appendix E

Asymptotic Expansions of  $Z_{\nu_m}(\kappa_n = \kappa_n \rho_0)$ 

In this Appendix, we derive asymptotic expressions of  $Z_{\nu_m}(\kappa_n a, \kappa_n \rho_0)$  and  $Z_{\nu_m}(\kappa_n a, \kappa_n \rho_0) H_{\nu_m}^{(2)}(\kappa_n \rho_0)$  where  $Z_{\nu_m}(\kappa_n a, \kappa_n \rho_0)$  is given by Eq. (7b) as

$$Z_{\nu_{m}}(\kappa_{n}^{a}, \kappa_{n}^{\rho_{0}}) = J_{\nu_{m}}(\kappa_{n}^{\rho_{0}}) - \frac{J_{\nu_{m}}(\kappa_{n}^{a})}{H_{\nu_{m}}^{(2)}(\kappa_{n}^{a})} H_{\nu_{m}}^{(2)}(\kappa_{n}^{\rho_{0}}).$$
 (E1)

For simplicity of notation, we write

$$\mathbf{x}_1 = \kappa_n \mathbf{a}$$
 (E2a)

$$\mathbf{x}_2 = \kappa_n \rho_0 \tag{E2b}$$

$$\nu = \nu_{\rm m}$$
 (E2c)

where

$$\kappa_{n} = \sqrt{k^{2} - k_{2n}^{2}}, I_{m}[\kappa_{n}] < 0.$$
 (E2d)

In this view, Eq. (E1) takes the form:

$$Z_{\nu}(x_1, x_2) = J_{\nu}(x_2) - \frac{J_{\nu}(x_1)}{H_{\nu}^{(2)}(x_1)} H_{\nu}^{(2)}(x_2)$$
 (E3a)

where

$$H_{\nu}^{(2)}(x) = J_{\nu}(x) - j Y_{\nu}(x).$$
 (E3b)

The asymptotic expansions of Eq. (ESa) will be derived in all relevant regions with respect to orders and arguments for both real and imaginary arguments.

## E1. REAL ARGUMENTS

# E1, 1 Debye's Asymptotic Expansion for Large Orders

If x is fixed and positive and  $\nu$  is large and positive, then from Eqs. (9.3.7), (9.3.8), and (9.3.9)?

$$J_{\nu}(x) \sim \frac{e^{-\nu\beta}}{\sqrt{2\pi\nu \tanh \alpha}} s_{j}$$
 (E4a)

$$Y_{\nu}(x) \sim -\sqrt{\frac{2}{\pi \nu \tanh \alpha}} e^{\nu \beta} s_{y}$$
 (E4b)

where

$$\beta = \alpha - \tanh \alpha \tag{E4c}$$

$$\alpha = \frac{1}{2} \ln \frac{1 + \sqrt{1 - (\frac{\pi}{2})^2}}{1 - \sqrt{1 - (\frac{\pi}{4})^2}}$$
 (E4d)

$$s_{j} = 1 + \sum_{k=1}^{\infty} \frac{u_{k} (coth\alpha)}{v^{k}}$$
 (E4e)

$$s_y = 1 + \sum_{k=1}^{\infty} (-1)^k \frac{u_k (coth \alpha)}{v^k}$$
 (E4f)

In Eqs. (E4e) and (E4f)

$$\mathbf{u_0} \ (\mathbf{t}) = \mathbf{1} \tag{E5a}$$

$$u_1(t) = \frac{3t - 5t^3}{24}$$
 (E5b)

$$u_2(t) = \frac{81 t^2 - 462 t^4 + 385 t^6}{1152}$$
 (E5c)

$$u_3(t) = \frac{30375 t^3 - 369603 t^5 + 765765 t^7 - 425425 t^9}{414720}$$
 (E5d)

$$u_{4}^{(t)} = \frac{4465125 t^{4} - 94121676 t^{6} + 349922430 t^{8} - 446185740 t^{10} + 185910725 t^{12}}{398 \ 13120}$$
 (E5e)

or in general

$$u_{k+1}(t) = \frac{1}{2}t^2(1-t^2)u_k(t) + \frac{1}{8}\int_0^t (1-5t^2)u_k(t) dt$$
,  $(k=0, 1, ...)$ . (E5f)

In terms of Bessel's function of first kind  $J_y(x)$  and Neumann functions,  $Y_y(x)$ ,  $Z_y(x_1, x_2)$  can be written in the form

$$Z_{\nu}(x_{1}, x_{2}) = J_{\nu}(x_{2}) - \frac{1}{F(x_{1})} \left[ \frac{J_{\nu}^{2}(x_{1})J_{\nu}(x_{2}) + J_{\nu}(x_{1}) Y_{\nu}(x_{1}) Y_{\nu}(x_{2})}{Y_{\nu}^{2}(x_{1})} + \frac{J_{\nu}(x_{1}) J_{\nu}(x_{2}) Y_{\nu}(x_{1}) - J_{\nu}^{2}(x_{1}) Y_{\nu}(x_{2})}{Y_{\nu}^{2}(x_{1})} \right]$$
(E6a)

where

$$F(x_1) = 1 + \frac{J_{\nu}^2(x_1)}{Y_{\nu}^2(x_1)}.$$
 (E6b)

Substitution of Eq. (E4) into Eq. (E6) yields

$$Z_{\nu}(x_{1}, x_{2}) = \frac{1}{\sqrt{2\pi\nu \tanh \alpha_{2}}} \left\{ s_{j2} e^{-\nu\beta_{2}} - \frac{1}{F(\beta_{1})} \left( \frac{s_{j1}}{s_{y1}} \right)^{2} \left[ \frac{s_{j2}}{4} e^{-\nu(4\beta_{1} + \beta_{2})} + \frac{1}{F(\beta_{1})} \left( \frac{s_{j1}}{s_{y1}} \right)^{2} \left[ \frac{s_{j2}}{4} e^{-\nu(4\beta_{1} + \beta_{2})} + \frac{1}{F(\beta_{1})} \left( \frac{s_{j1}}{s_{y1}} \right)^{2} \left[ \frac{s_{j2}}{4} e^{-\nu(4\beta_{1} + \beta_{2})} + \frac{1}{F(\beta_{1})} \left( \frac{s_{j1}}{s_{y1}} \right)^{2} \left[ \frac{s_{j2}}{4} e^{-\nu(4\beta_{1} + \beta_{2})} + \frac{1}{F(\beta_{1})} \left( \frac{s_{j1}}{s_{y1}} \right)^{2} \left[ \frac{s_{j2}}{4} e^{-\nu(4\beta_{1} + \beta_{2})} + \frac{1}{F(\beta_{1})} \left( \frac{s_{j1}}{s_{y1}} \right)^{2} \left[ \frac{s_{j2}}{4} e^{-\nu(4\beta_{1} + \beta_{2})} + \frac{1}{F(\beta_{1})} \left( \frac{s_{j1}}{s_{y1}} \right)^{2} \left[ \frac{s_{j2}}{4} e^{-\nu(4\beta_{1} + \beta_{2})} + \frac{1}{F(\beta_{1})} \left( \frac{s_{j1}}{s_{y1}} \right)^{2} \left[ \frac{s_{j2}}{4} e^{-\nu(4\beta_{1} + \beta_{2})} + \frac{1}{F(\beta_{1})} \left( \frac{s_{j1}}{s_{y1}} \right)^{2} \left[ \frac{s_{j2}}{4} e^{-\nu(4\beta_{1} + \beta_{2})} + \frac{1}{F(\beta_{1})} \left( \frac{s_{j1}}{s_{y1}} \right)^{2} \left[ \frac{s_{j2}}{4} e^{-\nu(4\beta_{1} + \beta_{2})} + \frac{1}{F(\beta_{1})} \left( \frac{s_{j1}}{s_{y1}} \right)^{2} \left[ \frac{s_{j2}}{4} e^{-\nu(4\beta_{1} + \beta_{2})} + \frac{1}{F(\beta_{1})} \left( \frac{s_{j1}}{s_{y1}} \right)^{2} \left[ \frac{s_{j2}}{4} e^{-\nu(4\beta_{1} + \beta_{2})} + \frac{1}{F(\beta_{1})} \left( \frac{s_{j1}}{s_{y1}} \right)^{2} \left[ \frac{s_{j2}}{4} e^{-\nu(4\beta_{1} + \beta_{2})} + \frac{1}{F(\beta_{1})} \left( \frac{s_{j1}}{s_{y1}} \right)^{2} \left[ \frac{s_{j2}}{4} e^{-\nu(4\beta_{1} + \beta_{2})} + \frac{1}{F(\beta_{1})} \left( \frac{s_{j1}}{s_{y1}} \right)^{2} \left[ \frac{s_{j2}}{4} e^{-\nu(4\beta_{1} + \beta_{2})} + \frac{1}{F(\beta_{1})} \left( \frac{s_{j1}}{s_{y1}} \right)^{2} \right] \right]$$

$$+\frac{s_{y1}s_{y2}}{s_{j1}}e^{-\nu(2\beta_{1}-\beta_{2})}+\frac{j}{2}\left(s_{y2}e^{-\nu(4\beta_{1}-\beta_{2})}-\frac{s_{y1}s_{j2}}{s_{j1}}e^{-\nu(2\beta_{1}+\beta_{2})}\right)\right\}$$
(E7a)

where asymptotic expansion of  $F(x_1)$  is

$$F(\beta_1) = 1 + \left(\frac{s_{j1}}{2 \cdot s_{y1}}\right)^2 e^{-4 \cdot \nu \beta_1}$$
 (E7b)

In Eq. (E7), subscripts 1 and 2 refer to arguments  $x_1$  and  $x_2$ , respectively. Similarly, one may write

$$Z_{\nu}(x_{1}, x_{2}) H_{\nu}^{(2)}(x_{2}) = J_{\nu}(x_{2}) Y_{\nu}(x_{2}) \left[ \frac{J_{\nu}(x_{2})}{Y_{\nu}(x_{2})} - j \right]$$

$$- \frac{1}{F(x_{1})} \left[ \frac{J_{\nu}^{2}(x_{1}) J_{\nu}^{2}(x_{2}) - J_{\nu}^{2}(x_{1}) Y_{\nu}^{2}(x_{2}) + 2J_{\nu}(x_{1}) J_{\nu}(x_{2}) Y_{\nu}(x_{1}) Y_{\nu}(x_{2})}{Y_{\nu}^{2}(x_{1})} + j \frac{J_{\nu}(x_{1}) J_{\nu}(x_{2}) Y_{\nu}(x_{1}) - 2J_{\nu}^{2}(x_{1}) J_{\nu}(x_{2}) Y_{\nu}(x_{2}) - J_{\nu}(x_{1}) Y_{\nu}^{2}(x_{2}) Y_{\nu}(x_{1})}{Y_{\nu}^{2}(x_{1})} \right] ( \mathbb{E} 36)$$

from where using Eq. (E4), the respective asymptotic expansion is

$$Z_{\nu}(x_{1}, x_{2}) H_{\nu}^{(2)}(x_{2}) = \frac{1}{\nu \pi \tanh \alpha_{2}} \left\{ \frac{s_{j2}^{2}}{2} e^{-2\nu \beta_{2}} + j s_{j2} s_{y2} - \frac{1}{F(\beta_{1})} \left( \frac{s_{j1}}{s_{y1}} \right)^{2} \left[ \frac{s_{j2}^{2}}{8} e^{-2\nu (2\beta_{1} + \beta_{2})} - \frac{s_{y2}^{2}}{2} e^{-2\nu (2\beta_{1} - \beta_{2})} + \frac{s_{j2} s_{y1} s_{y2}}{s_{j1}} e^{-2\nu \beta_{1}} + j \left( \frac{s_{j2} s_{y2}}{2} e^{-4\nu \beta_{1}} - \frac{s_{j2}^{2} s_{y1}}{4s_{j1}} e^{-2\nu (\beta_{1} + \beta_{2})} + \frac{s_{y1} s_{y2}^{2}}{s_{j1}} e^{-2\nu (\beta_{1} - \beta_{2})} \right) \right\}$$
(E8b)

where  $F(\beta_1)$  is given by Eq. (E7b). Note that  $\alpha_1 > \alpha_2$  since  $x_1 < x_2$ .

# E1.2 Limiting Forms for Small Arguments

In this section, we evaluate  $Z_{\nu}(x_1, x_2)$  and  $Z_{\nu}(x_1, x_2)$   $H_{\nu}^{(2)}(x_2)$  when  $x_1, x_2 \to 0$ . The expressions are applicable for  $0 \leqslant x_2 \leqslant 0.0001$ . Since

$$\kappa_n = k \sqrt{1 - \delta^2}$$
 (E9a)

one sees that when

$$\delta = \frac{k_{gn}}{k} \to 1$$

then  $\kappa_n \to 0$  and, consequently, as given by Eq. (E2a) and Eq. (E2b),  $\kappa_1 \kappa_2 \to 0$ . We distinguish two limiting cases:

(a) 
$$\nu = 0, x \to 0$$

In this case, from Abramowitz and Stegun (p. 360),  $^{7}$  when  $x \rightarrow 0$ 

$$J_0(x) \sim 1 \tag{E10a}$$

$$Y_0(x) \sim \frac{2}{\pi} \ln x \tag{E10b}$$

$$H_0^{(2)}(x) \sim -j \frac{2}{\pi} \ln x$$
 (E10c)

and therefore

$$\lim_{\substack{x_1, x_2 \neq 0}} Z_0(x_1, x_2) = \lim_{\substack{x_1, x_2 \neq 0}} \left[ J_0(x_2) - \frac{J_0(x_1) H_0^{(2)}(x_2)}{H_0^{(2)}(x_1)} \right]$$

= 1 - 
$$\lim_{\delta \to 1} \frac{4\pi (k\rho_0 \sqrt{1-\delta^2})}{4\pi (ka \sqrt{1-\delta^2})} = 0, \nu = 0.$$
 (E10d)

(b)  $\nu \neq 0$ , Re[ $\nu$ ] > 0,  $x \neq 0$ 

In this case, from Abramowits and Stegun<sup>7</sup> (p. 360), Bessel functions of the first kind, Neumann and Hankel functions can be expressed in terms of Gamma functions (see Abramowits and Stegun, <sup>7</sup> p. 255) as follows:

$$J_{\nu}(x) \sim \frac{\left(\frac{\pi}{2}\right)^{\nu}}{\Gamma(\nu+1)}. \tag{E11a}$$

$$Y_{\nu}(x) \sim -\frac{1}{\pi} \Gamma(\nu) \left(\frac{x}{2}\right)^{-\nu} \tag{E11b}$$

$$H_{\nu}^{(2)}(x) \sim j \frac{1}{\pi} f(\nu) \left(\frac{x}{2}\right)^{\nu}$$
 (E11c)

Substituting Eq. (E11) into Eq. (E3a), we get

$$\lim_{x_1, x_2 \to 0} Z_{\nu}(x_1, x_2) = \lim_{x_1, x_2 \to 0} \frac{1}{\Gamma(\nu + 1)} \left[ \left( \frac{x_2}{2} \right)^{\nu} - \left( \frac{x_1}{2} \right)^{2\nu} \left( \frac{x_2}{2} \right)^{-\nu} \right]$$

$$= \lim_{x_1, x_2 \to 0} \frac{1}{\Gamma(\nu+1)} \left(\frac{x_2}{2}\right)^{\nu} \left[1 - \left(\frac{x_1}{x_2}\right)^{2\nu}\right]$$

$$= \frac{1}{\Gamma(\nu+1)} \lim_{\delta \to 1} \left(\frac{k\rho_0 \sqrt{1-\delta^2}}{2}\right)^{\nu} \left[1 - \left(\frac{ka\sqrt{1-\delta^2}}{k\rho_0 \sqrt{1-\delta^2}}\right)^{2\nu}\right] = 0, \ \nu \neq 0. \ (E12)$$

We follow the same procedure to evaluate  $\lim_{x_1, x_2 \to 0} Z_y(x_1, x_2) H_y^{(2)}(x_2)$ .

Namely,

(a) 
$$y = 0, x \to 0$$

Using Eq. (E11), we have

$$\lim_{x_1, x_2 \to 0} Z_0(x_1, x_2) H_0^{(2)}(x_2) = -j \frac{2}{\pi} \lim_{x_1, x_2 \to 0} \left(1 - \frac{4\pi x_2}{4\pi x_1}\right) 4\pi x_2$$

$$= -j \frac{2}{\pi} \lim_{x_1, x_2 \to 0} An \frac{x_1}{x_2} \frac{An x_2}{An x_1} = -j \frac{2}{\pi} \lim_{\delta \to 1} An \frac{\ln \sqrt{1 - \delta^2}}{\ln \rho_0 \sqrt{1 - \delta^2}} \frac{An \ln \rho_0 \sqrt{1 - \delta^2}}{An \ln \sqrt{1 - \delta^2}}.$$

$$= -j\frac{2}{\pi} 4n \frac{ka}{k\rho_0} \lim_{\delta \to 1} \frac{4n k\rho_0 \sqrt{1-\delta^2}}{4n ka \sqrt{1-\delta^2}} = -j\frac{2}{\pi} \ln \frac{ka}{k\rho_0}, \quad \nu = 0$$
 (E13)

In this case, using Eq. (E11) from Eq. (E3a)

$$\lim_{x_1, x_2 \to 0} Z_{\nu}(x_1, x_2) H_{\nu}^{(2)}(x_2) = \lim_{x_1, x_2 \to 0} \left[ \frac{\left(\frac{x_2}{2}\right)^{\nu}}{\Gamma(\nu+1)} \frac{\left(\frac{x_1}{2}\right)^{\nu} \left(\frac{x_2}{2}\right)^{-\nu}}{\Gamma(\nu+1) \left(\frac{x_1}{2}\right)^{-\nu}} \right]$$

$$\frac{\mathrm{j}}{\pi}\Gamma(\nu)\left(\frac{\mathrm{x_2}}{2}\right)^{-\nu} = \frac{\mathrm{j}}{\pi\Gamma(\nu+1)}\frac{\Gamma(\nu)}{\delta+1}\left[1-\left(\frac{\mathrm{kz}\sqrt{1-\delta^2}}{\mathrm{k}\rho_0\sqrt{1-\delta^2}}\right)^{2\nu}\right]$$

$$= \frac{j}{\pi} \frac{\Gamma(\nu)}{\Gamma(\nu+1)} \left[ 1 - \left( \frac{ka}{k\rho_0} \right)^{2\nu} \right]. \tag{E14}$$

Utilizing identities

$$\Gamma(\nu+1)=\nu! \tag{E15a}$$

$$\Gamma(\nu) = (\nu - 1)! \tag{E15b}$$

$$\frac{\Gamma(\nu)}{\Gamma(\nu+1)} = \frac{1}{\nu} \tag{E15c}$$

we obtain

$$\lim_{\mathbf{x}_{1}, \mathbf{x}_{2} \to 0} Z_{\nu}(\mathbf{x}_{1}, \mathbf{x}_{2}) H_{\nu}^{(2)}(\mathbf{x}_{2}) = \frac{j}{\pi \nu} \left[ 1 - \left( \frac{ka}{k \rho_{0}} \right)^{2 \nu} \right]. \tag{E15d}$$

# **E2. IMAGINARY ARGUMENTS**

When  $k_{zn}^{2} > k^{2}$  in Eq. (E2d), then

$$\kappa_{n} = -j \sqrt{k_{2n}^2 - k^2} = -j |\kappa_{n}|. \tag{E16}$$

We set

$$\mathbf{x}_{1} = |\kappa_{n}|^{2}$$

$$\mathbf{x}_2 = |\kappa_n| \rho_0 \tag{E17b}$$

where  $x_1$  and  $x_2$  are real. Using Eqs. (9.6.3) and (9.6.4)

$$J_{\nu}(-jx) = e^{-j\frac{\pi}{2}\nu} I_{\nu}(x)$$
 (B18a)

$$H_{\nu}^{(2)}(-jx) = j\frac{2}{\pi}e^{j\frac{\pi}{2}\nu}K_{\nu}(x)$$
 (E18b)

where  $I_{\nu}(x)$  and  $K_{\nu}(x)$  are Modified Bessel functions,  $Z_{\nu}(x_1, x_2) H_{\nu}^{(2)}(x)$  becomes

$$Z_{\nu} \left(-jx_{1}, -jx_{2}\right) H_{\nu}^{(2)} \left(-jx_{2}\right) = j\frac{2}{\pi} \left[ I_{\nu}(x_{2}) - \frac{I_{\nu}(x_{1})}{K_{\nu}(x_{1})} K_{\nu}(x_{2}) \right] K_{\nu}(x_{2}). \quad (E18c)$$

In the following two sections, we expand Eq. (E18c) in the asymptotic series.

# E2.1 Asymptotic Expansions for Large Arguments

When  $\nu$  is fixed, |x| is large from Eqs. (9.7.1) and (9.7.2)

$$I_{\nu}(x) \sim \frac{e^{x}}{\sqrt{2\pi x}} s_{i} \left( \left| \arg x \right| < \frac{\pi}{2} \right)$$
 (E19a)

$$K_{\nu}(x) \sim \sqrt{\frac{\pi}{2x}} e^{-x} s_{k} (|\arg x| < \frac{3\pi}{2})$$
 (E19b)

where

$$\mathbf{s_i} = 1 - \frac{\mu - 1}{8\mathbf{x}} + \frac{(\mu - 1)(\mu - 9)}{2! (8\mathbf{x})^2} - \frac{(\mu - 1)(\mu - 9)(\mu - 25)}{3! (8\mathbf{x})^3} + \dots$$
 (E19c)

$$\mathbf{s_k} = 1 + \frac{\mu - 1}{8\mathbf{x}} + \frac{(\mu - 1)(\mu - 9)}{2!(8\mathbf{x})^2} + \frac{(\mu - 1)(\mu - 9)(\mu - 25)}{3!(8\mathbf{x})^3} + \dots$$
 (E19d)

and

$$\mu = 4\nu^2 . ag{E19e}$$

Using Eq. (E19), we have

$$\left[I_{\nu}(\mathbf{x}_{2}) - \frac{I_{\nu}(\mathbf{x}_{1})}{K_{\nu}(\mathbf{x}_{1})} K_{\nu}(\mathbf{x}_{2})\right] K_{\nu}(\mathbf{x}_{2}) = \frac{1}{2\mathbf{x}_{2}} (\mathbf{s}_{12} \, \mathbf{s}_{k2} - \frac{\mathbf{s}_{11} \, \mathbf{s}_{k2}^{2}}{\mathbf{s}_{k1}} \, \mathbf{e}^{-2(\mathbf{x}_{2} - \mathbf{x}_{1})} \quad (E20)$$

where again subscripts 1 and 2 are associated with arguments  $x_1$  and  $x_2$ , respectively.

## E2.2 Uniform Asymptotic Expansions for Large Orders

From Eqs. (9.7.7) and (9.7.8)

$$I_{\nu}(x) \sim \frac{1}{\sqrt{2\pi\nu}} \frac{e^{\nu\eta}}{(1+x^2)^{1/4}} s_i$$
 (E21a)

$$K_{\nu}(x) \sim \sqrt{\frac{\pi}{2\nu}} \frac{e^{-\nu\eta}}{(1+x^2)^{1/4}} s_k$$
 (E21b)

where

$$\mathbf{s_i} = 1 + \sum_{k=1}^{\infty} \frac{\mathbf{u_k}(t)}{\nu^k}$$
 (E21c)

$$s_k = 1 + \sum_{k=1}^{\infty} (-1)^k \frac{u_k(t)}{u^k}$$
 (E31d)

When  $\nu \to +\infty$ , these expansions hold uniformly with respect to x in the sector  $|\arg x| \le \pi/2 - \epsilon$ , where  $\epsilon$  is an arbitrary positive number. Here

$$t = \frac{1}{\sqrt{1 + x^2}} \tag{E22a}$$

$$\eta = \sqrt{1 + x^2} + 4n \frac{x}{1 + \sqrt{1 + x^2}}$$
 (E22b)

and  $u_k(t)$  are given by Eq. (E5).

Using Eq. (E21) to Eq. (E22), we can write

$$\left[I_{\nu}(x_{2}) - \frac{I_{\nu}(x_{1})}{K_{\nu}(x_{1})}K_{\nu}(x_{2})\right] K_{\nu}(x_{2}) = \frac{1}{2\nu} \frac{1}{\sqrt{1+x_{2}^{2}}} \left[s_{12} s_{k2}\right]$$

$$-\frac{s_{11} s_{k2}^2}{s_{k1}} e^{-2\nu(\eta_2 - \eta_1)}$$
(E33a)

where

$$\eta_2 - \eta_1 = \sqrt{1 + x_2^2} - \sqrt{1 + x_1^2} + 4\eta \frac{x_2 (1 + \sqrt{1 + x_2^2})}{x_1 (1 + \sqrt{1 + x_2^2})}$$
(E335)

# E2.3 Limiting Forms for Small Arguments

Here we evaluate

$$\lim_{\mathbf{x_1},\,\mathbf{x_2} \to 0} \left[ \mathbf{I}_{\nu}(\mathbf{x_2}) - \frac{\mathbf{I}_{\nu}(\mathbf{x_1})}{\mathbf{K}_{\nu}(\mathbf{x_1})} \, \mathbf{K}_{\nu}(\mathbf{x_2}) \right] \mathbf{K}_{\nu}(\mathbf{x_2})$$

where, again, we distinguish two cases:

(a) 
$$\nu = 0$$
,  $x + 0$   
Using Eqs. (9.6.7) and (9.6.8)<sup>7</sup>

$$I_0(x) \sim 1 \tag{E24a}$$

$$K_0(x) \sim -4n x$$
 (E24b)

one sees that

$$\lim_{\delta \to 1} \left[ 1 - \frac{4 \ln k \rho_0 \sqrt{\delta^2 - 1}}{4 \ln k a \sqrt{\delta^2 - 1}} \right] (-4 \ln k \rho_0 \sqrt{\delta^2 - 1})$$

$$= -\ln \frac{ka}{k\rho_0} \lim_{\delta \to 1} \frac{\ln k\rho_0 \sqrt{\delta^2 - 1}}{\ln ka \sqrt{\delta^2 - 1}} = -\ln \frac{ka}{k\rho_0}.$$
 (E24c)

(b)  $\nu \neq 0$ ,  $x \neq 0$ In this case, from Eqs. (9.6.7) and (9.6.9)<sup>7</sup>

$$I_{\nu}(\mathbf{x}) \sim \frac{\left(\frac{\mathbf{x}}{2}\right)^{\nu}}{\Gamma(\nu+1)}$$
 (E25a)

$$K_{\nu}(x) \sim \frac{1}{2} \left(\frac{x}{2}\right)^{\nu} \Gamma(\nu)$$
 (E25b)

and consequently

$$\lim_{\mathbf{x}_1, \, \mathbf{x}_2 \to 0} \, \left[ \mathbf{I}_{\nu}(\mathbf{x}_2) \, - \frac{\mathbf{I}_{\nu}(\mathbf{x}_1)}{\mathbf{K}_{\nu}(\mathbf{x}_1)} \, \mathbf{K}_{\nu}(\mathbf{x}_2) \right] \, \mathbf{K}_{\nu}(\mathbf{x}_2)$$

$$= \lim_{x_{1}, x_{2} \to 0} \frac{\left[\left(\frac{x_{2}}{2}\right)^{\nu}\right] - \left(\frac{x_{1}}{2}\right)^{\nu}\left(\frac{x_{2}}{2}\right)^{-\nu}}{\Gamma(\nu+1)\left(\frac{x_{1}}{2}\right)^{-\nu}} \frac{1}{2}\Gamma(\nu)\left(\frac{x_{2}}{2}\right)^{-\nu}$$

$$= \frac{1}{2} \frac{\Gamma(\nu)}{\Gamma(\nu+1)} \lim_{x_1, x_2 \to 0} \left[ 1 - \left(\frac{x_1}{2}\right)^{2\nu} \left(\frac{x_2}{2}\right)^{-2\nu} \right] =$$

$$= \frac{1}{2\nu} \lim_{\delta \to 1} \left[ 1 - \left( \frac{\ln \sqrt{\delta^2 - 1}}{\ln \rho_0 \sqrt{\delta^2 - 1}} \right)^{2\nu} \right] - \frac{1}{2\nu} \left[ 1 - \left( \frac{\ln \delta}{\ln \rho_0} \right)^{2\nu} \right].$$
 (E25c)

Appendix F

The far field due to a singly excited element in a match-terminated vironment is given by Eq. (31b) as

$$\mathbf{E}_{\theta}^{(e)}\left(\mathbf{r},\,\theta\,,\,\phi\right) = \sqrt{\frac{\xi}{4\pi Z_{1}}} \,\,\mathbf{V}_{inc} \,\,\frac{e^{-j\mathbf{k}\mathbf{r}}}{\mathbf{r}} \,\,\mathbf{g}_{\theta}^{(e)}\left(\theta,\,\phi\right). \tag{F1}$$

The phase reference point is at r = 0, that is, at the origin of the cylindrical coordinate system  $(\rho, \phi, z)$  shown in Figures 1 and 2. It was found that the flattest element pattern phase in the broadside region is obtained when the phase reference point is at  $(\rho_{\rm ph} = a + 0.8s, \theta = 90^{\circ}, \phi = 0^{\circ})$  that is, 0.2s below the dipole center. Therefore, it is desirable to represent the far field at  $(r, \theta, \phi)$  with respect to the new phase reference point ( $\rho_{\rm ph}$ ,  $\theta$  = 90°,  $\phi$  = 0°). Denoting this field by  $E_{\theta}$  (R,  $\theta$ ,  $\phi$ ) where

$$R = r - \rho_{\rm ph} \sin \theta \cos \phi \tag{F2a}$$

is the distance between the new phase reference point ( $\rho_{\rm ph}$ ,  $\theta$  = 90°,  $\phi$  = 0°) the field observation point  $(r, \theta, \phi)$ , we may write

$$E_{\theta}^{(e)}(R, \theta, \phi) \simeq E_{\theta}^{(e)}(r, \theta, \phi) e^{jk\rho_{ph} \sin \theta \cos \phi}$$
 (F2b)

and  $E_{\theta}^{(e)}$  (r,  $\theta$ ,  $\phi$ ) is given by Eq. (F1). In Eq. (F2b), we assumed that, so far as amplitude of the field is concerned,  $1/r \simeq 1/R$ .

Substitution of Eq. (F1) into Eq. (F2b) yields

$$E_{\theta}^{(e)}(R, \theta, \phi) = \sqrt{\frac{\zeta}{4\pi Z_1}} V_{inc} \frac{e^{-jkr}}{r} g_{\theta}^{(e)}(\rho_{ph}; \theta, \phi)$$
 (F3a)

where

$$g_{\theta}^{(e)}(\rho_{\text{ph}}; \theta, \phi) = g_{\theta}^{(e)}(\rho_{\text{ph}} = 0; \theta, \phi) e^{-jk \rho_{\text{ph}} \sin \theta \cos \phi}$$
 (F3b)

and

$$g_{\theta}^{(e)}(\rho_{ph}=0;\theta,\phi)=g_{\theta}^{(e)}(\theta,\phi).$$
 (F3c)

# Element Pattern of an Axial Dipole in a Cylindrical Phased Array, Part 2: Element Design and Experiments

## 1. INTRODUCTION

This part describes the experimental effort and presents measured data that strongly support the validity of the theoretical model over a meaningfully large range of element and array parameters. These experiments are in support of theoretical work presented previously (see also Part 1).

The array construction is described in Section 2, followed by the design and matching of the folded dipole radiator in Section 3. Experimental amplitude element patterns are presented in Section 4 with theoretical results superimposed, showing good agreement in spite of the fact that the theory addresses a simple dipole and the measurements were performed on a folded dipole. Measurements substantiating the theoretical results obtained for the element phase pattern are discussed in Section 5. Array beam forming effects are briefly considered in Section 6 along with polarization purity. The influence of dipole feed line interactions on the radiation pattern are pointed out.

<sup>(</sup>Received for publication 31 January 1984)

Herper, J.C., Hessel, A., and Tomasic, B. (1985) Element pattern of an axial dipole in a cylindrical phased array, Part 1: Theory, Part 2: Element design and experiments, <u>IEEE Trans. Antennas Propag.</u>, AP-33.

#### 2. ARRAY DESCRIPTION

An experimental test bed was fabricated to investigate the sidelobe and azimuth phase scan capabilities of cylindrical array antennas. This array was used to measure the element patterns over a frequency range that exceeded the component design bandwidth. The array is described in this section, including the feed network and dipole geometry.

The array consists of 80 axial column networks covering a 150° arc of a cylinder as shown in Figure 1. The diameter (2a) of the cylinder at the dipole ground plane is 29 wavelengths (all dimensions, unless stated otherwise, are referenced to the center frequency  $f_c$ ). The column networks extend approximately 15 wavelengths, with 22 axial dipoles spaced at 0.67 wavelength. This corresponds to an elevation incipient endfire grating lobe angle of 24° at the high end of the  $\pm$ 6 percent operating band for which the array had been designed. The column networks are assembled into an array with a locally rectangular lattice having circumferential spacing of 0.5 wavelength at the high end of the frequency band. This spacing was chosen to provide adequate suppression of the wide angle circumferential grat-

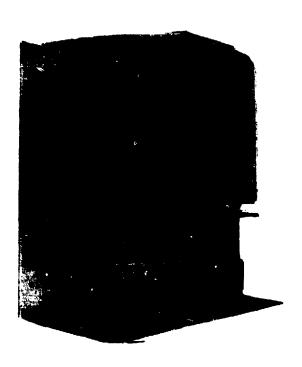


Figure 1. Cylindrical Array Test Bed Antenna

ing lobes characteristic of fully excited cylindrical arc arrays with large aperture utilization. <sup>2</sup>

The column networks are microwave printed circuits of two types. The first type consists of 22 axially polarised folded dipole arediating elements, each fed by a half-wavelength differential line length balun and matched to its own input line by a multiple step transformer. These radiators are used to measure patterns in the conventional manner on a far field range. The other type of column network incorporates a microwave printed circuit that generates an axial illumination taper function for low sidelobe patterns. This type of network, originally designed for the array studies, is useful for measuring circumferential element patterns through the Exial beam peak by virtue of its increased isolation from ground reflections on the measurement range. Also, increased line source gain over that of the single dipole improves the measured signal-to-noise ratio permitting circumferential patterns to be measured to large angles before becoming noise limited. The measured noise level of the single dipole element patterns is approximately 10dB poorer than the noise of the column patterns, in good agreement with the gain improvement. Except for the noise level, measurements with both types of networks for the same conditions provided identical results.

The column networks utilize the folded dipoles and baluns discussed above. fed by a 22:1 corporate power divider designed to produce a -35dB Taylor illumination using compensated Wilkinson couplers. The symmetric and four-port resistive nature of these coupler makes them particularly useful. They provide a uniform power split in amplitude and phase as a function of frequency, excellent wideband match, and high isolation. Each of the dipoles and the column network input is effectively isolated from the mismatches created at other dipoles during variations of scan and frequency. As a result, any dipole in the array sees an excellent feed match over all scan and frequency conditions. The printed circuits are copper-clad Kapton, sandwiched between aluminum ground planes using low dielectric constant foam spacers. The response of the couplers and transmission lines is flat in amplitude and phase over the 12 percent operating band. Measurements on the 80 column networks over the operating band showed rms phase and amplitude tolerances of 2.1° and 0.15 dB, respectively. A picture of the network is shown in Figure 2 with the protective foam partially removed to display the dipoles.

<sup>2.</sup> Hessel, A. (1972) Mutual coupling effects in circular arrays on cylindrical surfaces - aperture design implications and analysis, Phased Array Antennas, Artech House, Dedham, Mass., p. 273.

<sup>3.</sup> Jasik, H. (1959) Antenna Engineering Handbook, McGraw-Hill, New York, p. 3-13 to 3-15.

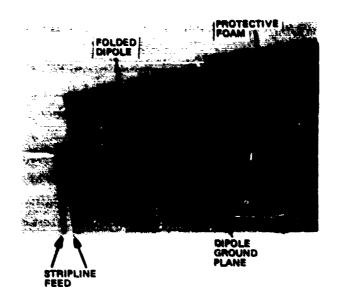


Figure 2. Column Network With Protective Foam Partially Removed Showing Dipole Radiators

## 3. DIPOLE DESIGN

A folded dipole fed by a differential line length balun was chosen because of its extensive use in planar arrays and good correlation to theoretical performance for those applications. A previously used design was scaled to the desired operating band, and the element was matched in a planar waveguide simulator using both reflection and transmission measurements. An outline diagram of the radiator is shown in Figure 3. The dipole is 0.42 wavelength long and is located at 0.24 wavelength above the cylindrical ground at center frequency. It is fed by a two-wire line in the free space region and matched to two stripline conductors of the same impedance. The balun is formed in this stripline by adding a half-wavelength of line on one feed. The two lines are then reactively combined into a  $70\,\Omega$  characteristic impedance stripline used for the remainder of the printed circuitry.

As described by Jasik, <sup>3</sup> the folded dipole performs in a fashion similar to the ordinary center-fed dipole with the folded lines providing an impedance transformer between the dipole and its feed line. The nearest to broadside single-element, single-mode 45° H-plane simulator shown in Figure 4a was employed for matching the dipole. The simulator was excited at the end opposite the dipole with an orthogonal mode transducer. This provided a convenient means to measure and/or terminate the cross-polarized radiation. Also shown in Figure 4b is a test dipole in its mating ground plane fixture. Figure 4c is a diagram of the element lattice. For this configuration, the simulator height is the same as the

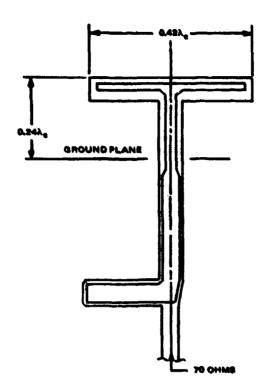


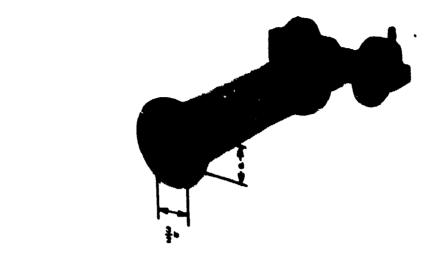
Figure 3. Outline Diagram of Folded Dipole Radiator With Stripline Feed

axial dipole spacing and the simulator width is 50 percent greater than the circumferential dipole spacing. The dipole is located one-third the simulator width from the left side wall. The simulator is exact for an element in a planar array. It approximates the active dipole impedance at the average scan in the arc excited for broadside beam formation in a large cylindrical array. The resulting impedance match over the ± 6 percent design operating band is shown in Figure 5. A voltage standing-wave ratio (VSWR) of better than 1.3:1 was achieved over the operating band.

#### 4. MEASURED AMPLITUDE PATTERNS

Dipole element amplitude patterns were measured on a 675-ft antenna range. Extensive measurements were performed in the ± 6 percent design operating band. Selected measurements were also made up to 30 percent above the design operating frequency. All measured dipole patterns correlated very well with the theoretically predicted performance.

The experimental data required somewhat modified computations compared to those presented. First, since the experimental dipole is matched at 0° in the



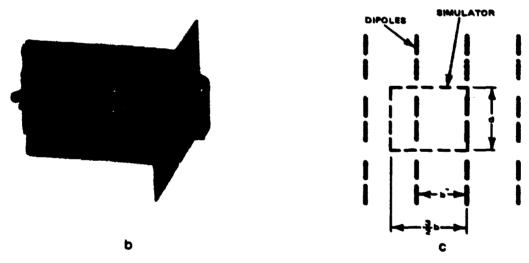


Figure 4. Waveguide Simulator for 45° H-Plane, 0°, E-Plane Scan.
(a) Simulator body with orthogonal moade transducer. (b) Test dipole in fixture. (c) Relationship of array lattice to simulator size and location

E-plane and 45° in the H-plane, the theoretical data shown here were recomputed to reflect this condition. In general, this effect causes a reflection mismatch of about 0.5 dB at broadside, which flattens the central portion of the pattern out to the match angle and slightly narrows the patterns for angles greater than the match angle. The second change incorporated into the computer simulation arises from the fact that, in the experiments, the physical dimensions are held constant

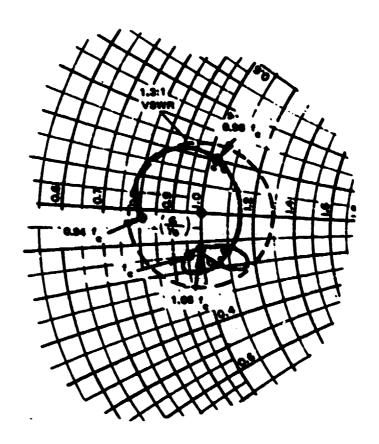


Figure 5. Measured Dipole Impedance in Waveguide Simulator

while the frequency varies. This leads to a set of normalized element and array dimensions that increase linearly with the impressed source frequency. Tables are provided on each pattern indicating the normalized dimensions of the antenna at the measurement frequencies. The symbols are defined in a list at the end of this report.

The measured H-plane pattern at the center frequency ( $f = f_C$ ) is shown as the solid curve in Figure 6. This condition corresponds to a circumferential spacing between dipoles of 0.48 wavelength. The curve shows the element gain in dB normalized to that of the unit cell area versus the circumferential field angle  $\phi$  measured from the element broadside as the abscissa. This is a principal H-plane column pattern (taken normal to the cylinder axis, that is, at  $\phi = 90^\circ$  with respect to the cylinder axis). Measurements were terminated at -40 dB below the beam peak ( $\phi = \pm 120^\circ$ ) because of test and site instrumentation noise limitations. Superimposed on this plot are theoretical points represented by dots. The excellent agreement is evident; this, in spite of the fact that the theoretical model employs a simple strip dipole of negligible radial thickness, while the actual folded dipole is

printed on radial boards. The length L of the theoretical model was assumed equal to that of the top arm of the folded dipole.

A similar set of data at a frequency 4 percent higher showing excellent correlation between experiment and theory is shown in Figure 7. This result is of in-

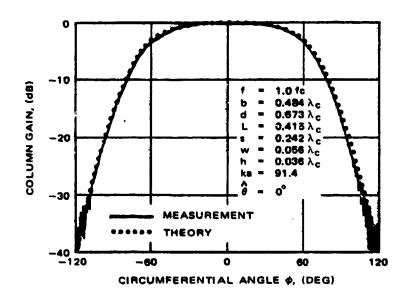


Figure 6. Measured and Theoretical Amplitude Patterns at Center Frequency

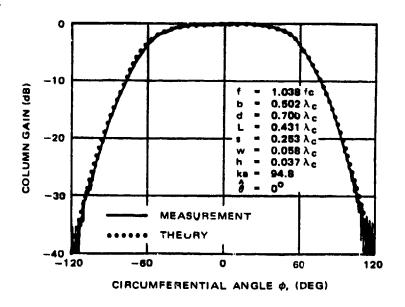


Figure 7. Amplitude Patterns 4 Percent Above Center Frequency

terest for comparison to slot data provided in the literature. <sup>4</sup> This frequency provides an effective element spacing of 0.50 wavelength. In contrast to a slot array with this spacing, the dipole patterns show no discernible element pattern ripples in the forward region. For further comments in this connection, see Part 1 of this report.

Data for a circumferential element spacing of 0.594 wavelength at  $f = 1.2f_C$ , is shown in Figure 8. To accentuate the pattern ripple in the lit region, this graph is plotted with the ordinate on a linear (voltage) scale, again normalized to the unit cell gain. Correlation of the experimental data (solid curve) with the theory (dots) is again remarkably good, especially since the test frequency is more than 20 percent above the center frequency at which the components were designed to operate.

A series of measurements presented in Figure 9 shows the dipole pattern performance parametrically at a number of conical cut angles relative to the cylinder axis. These patterns are for polar angles  $\theta$  of 90° (Figure 9a), 80° (Figure 9b),

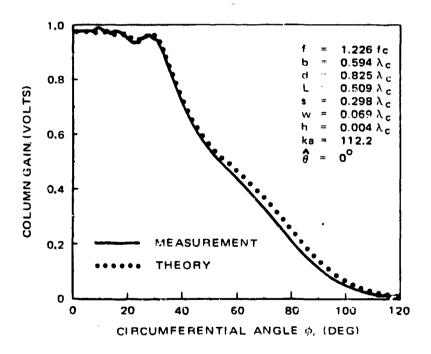
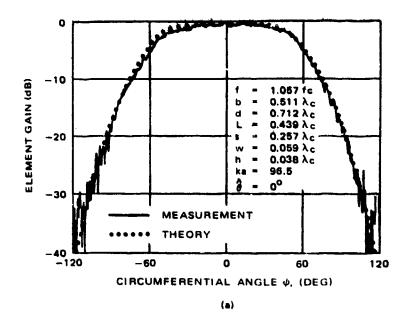


Figure 8. Amplitude Patterns 22.6 Percent Above Center Frequency

<sup>4.</sup> Sureau, J.C., and Hessel, A. (1971) Element pattern for circular arrays of waveguide-fed axial slits on large conducting cylinders, <u>IEEE Trans. Antennas Propag.</u> AP-19:64-76.



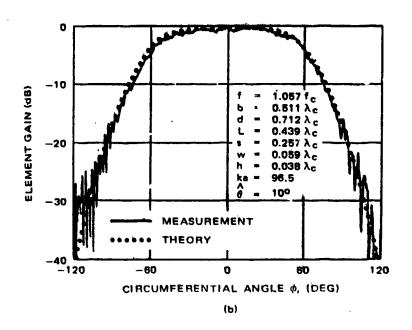
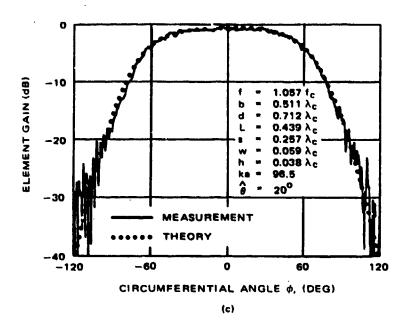


Figure 9. Amplitude Patterns at Various Elevation Angles. (a)  $\theta = 0^{\circ}$ . (b)  $\theta = 10^{\circ}$ 

70° (Figure 9c), and 60° (Figure 9d). In contrast to the previous patterns, which were column patterns, these element patterns are of lower absolute gain by about 10 cB and are thus affected by measurement system noise at a 10 dB higher level. Perk gain decreases with elevation angle at nearly a cosine voltage pattern as expected for an E-plane dipole scan when both the unit cell directivity and scan mis-



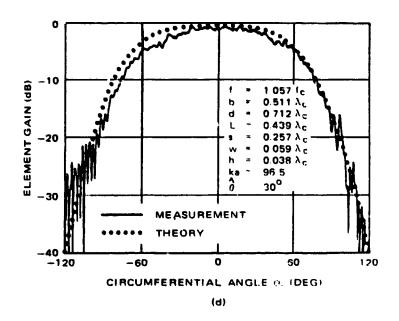


Figure 9 (cont.). Amplitude Patterns at Various Elevation Angles. (c)  $\theta = 20^{\circ}$ . (d)  $\theta = 30^{\circ}$ 

match gain loss are included. The patterns show a general circumferential broadening with increasing elevation scan. As indicated by the superimposed dots, the actual performance is very close to the theoretically predicted performance.

#### 5. PHASE PERFORMANCE

In Part 1 of this report, the phase response of the dipole was found to be flat to within a few degrees over a large portion of the lit region when the phase reference distance from the ground plane is taken about 80 percent of the distance from the ground to the dipole strip. Instead of measuring the element phase directly, a rather difficult undertaking on a far-field range, an indirect focusing measurement was performed.

The focusing experiment consists of the following tasks. A convenient illumination function is impressed on the array. Far-field patterns are measured as the element phase excitation is varied by incrementing the apparent radius of the cylindrical array illumination. This simulates the variation of the dipole phase center location. An error in the phase center location impresses a quadratic phase error on the array collimation which, in turn, manifests itself as pattern defocusing. From a practical viewpoint, approximately the same results may be obtained more easily by varying the test frequency without readjusting the array collimation. This effectively simulates the desired collimation variation.

The experiment begins with the radius set to the actual dipole location. As the radius (equivalent dipole radial distance) is reduced, the nulls of the close-in sidelobes increase in depth, indicating an improvement in the array focusing. For a radius corresponding to 70 percent of the distance from the ground plane to the dipole, these nulls reach maximum depth. Null depths at this point are about 15 dB better than at the beginning of the experiment. Further reduction of the radius only degrades the null depths, confirming that the optimum location has been exceeded. These measured results are shown graphically in Figure 10.

The theoretically predicted phase center location thus agrees very well with the results of the focusing measurement. This good focus held over a ± 6 percent test band and with circumferential phase s an of the array. The agreement with theory is further accentuated since the folded dipole feed employed in the measurements can be expected to have a slightly different phase center location than the flat strip dipole investigated in the theory.

#### 6. ARRAY BEAM FORMING CONSIDERATIONS

An important effect in cylindrical arrays is the formation of residual deleterious grating lobes. This effect is caused by the edge subarrays of the aperture, which need to be given large progressive phase delays to collimate the beam and which have large enough spacing to generate a grating lobe. Using the precise element patterns generated by the methods described in Part 1, the grating lobes

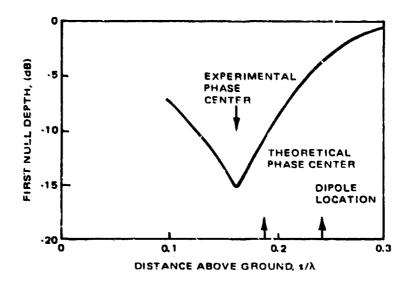


Figure 10. Location of Dipole Phase Center

can be accurately predicted. These lobes generally occur at azimuth angles greater than 90° from broadside, may have large amplitude compared with the desired sidelobe levels, and are usually very broad in angular extent. These effects are demonstrated in the literature. 2,5,6 The one, design tool effective in controlling these grating lobes is the reduction of the circumferential spacing between the elements of the array. Figure 11 shows the result of a parametric study of this effect. A cylinder of constant radius (ka = 140) is considered, and the grating lobe level is plotted versus circumferential element spacing. A 120° sector of the array is assumed to be excited with a low sidelobe illumination at broadside and . 15° circumferential phase scan, which corresponds to 75° scan for the edge element. When the beam is broadside to the excited aperture, the far out sidelobes computed in the region where the grating lobe appears approached -70 dB for close element spacings. For element spacing near 0.50 wavelength, the residual grating lobe level generated is negligible. As the element spacing approaches 0.60 wavelength, lobes well above -40 dB (relative to the main beam) are produced. For many applications, such grating lobe levels would be unacceptable.

Another deleterious mutual coupling and curvature effect, discussed in Part 1 of this report, results from the behavior of the element pattern as a function of element spacing. At element circumferential spacings corresponding to 0.5 wave-

<sup>5.</sup> Sureau, J.C., and Hessel, A. (1972) Realized gain function for a cylindrical array of open-ended waveguides, <u>Phased Array Antennas</u>, Artech House, Dedham, Mass., p. 315.

<sup>6.</sup> Provencher, J.H. (1972) Conformal arrays on surfaces with rotational symmetry, Phased Array Antennas, Artech House, Dedham, Mass., p. 301.

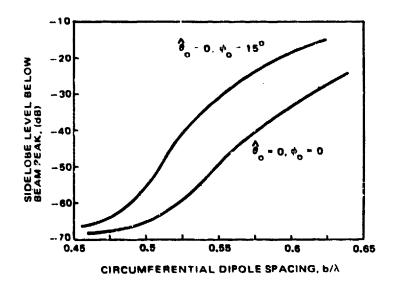


Figure 11. Grating Lobe Level of a Low Sidelobe Pattern Excited by a 120° Cylindrical Array Arc

length, a smooth dipole pattern is observed. For spacings greater than this, a ripple, due to creeping waves propagating around the cylinder, appears in the broadside region of the element pattern. In a cylindrical array, this ripple can act like a periodic error across the array, and, at some frequencies, may lead to the generation of anomalies in the near-in array sidelobes. Indeed, element ripple levels of a few tenths of a dB peak-to-peak could cause sidelobe peaks on the order of -40 dB below the array beam peak. This effect on the sidelobe level is generally difficult to predict because it depends on the proper correlation of the periodicity of the element pattern ripple with the effective element spacing, each of which depends on frequency. Many frequency patterns must be evaluated to guarantee suppression of this effect to acceptable levels. If measured patterns are employed to predict array performance, care must be exercised in separating the actual ripples obtained on a full cylindrical array from those caused by experimental anomalies such as range multipath or edge effects due to finite subarray test units.

It is also useful to compare the dipole performance with that of a slot radiator. <sup>4</sup> For equivalent size cylinders and element spacings, the dipole has considerably less pattern ripple than the slot. This is attributed to the imaging property of the dipole above its ground (see Part 1 of this report). Also, the dipole has a slightly broader pattern due to the weaker grating lobe effect as compared to the slot. These features may favor the dipole in array designs that utilize significant portions of a cylindrical arc or where low sidelobes are desired.

As discussed in Part 1 of this report, the longitudinal current approximation for the axial strip dipole does not predict any circumferential far E-field. Array

pattern measurements confirm this analysis. The cross-polarization was measured over a large region about the beam in the circumferential, axial, and skew planes. The cross-polarization level was everywhere better than 10 dB below the corresponding co-polarization level at the same angle and was generally as good as the cross-polarized level of the site transmit dish. Thus, no experimental evidence exists for coupling to the cross-polarized radiation within the measurement region. This indicates that other structures such as the feed lines and the folded feed that could couple to the cross-polarized radiation generate no significant circumferential electric field.

It has been noted in the literature that, under certain circumstances, the dipole feed lines can resonate with the dipole to form pattern blind spots in the Eplane. 7,8 Data and discussion of this effect are scanty, difficult to obtain, and often limited to verbal presentations. Pattern data in the axial (E) plane were limited to 30° because of turntable loading considerations. No resonance effects were encountered out to this point.

## 7. CONCLUSION

The measured results for the element pattern of an axial dipole element in a cylindrical phased array lead us to the following conclusions:

- 1. The modal analysis developed in Part 1 of this report agrees very well with the measured data indicating that the method and the numerical results are very accurate.
- 2. The assumption that the feed lines have little effect is justified. For the scans and frequencies investigated, no differences were discernible between the theory (no feed modeled) and the experiments with the folded end-fed dipole and two-wire-line feed.
- 3. A high polarization purity and wide bandwidth dipole and feed are achievable.
- 4. The accurate knowledge of element pattern amplitude and phase afforded by this method makes possible the precise prediction of cylindrical array performance over a full 360° azimuth range.

<sup>7.</sup> Reale, J.D. (1974) PAR hardened cross-dipole array (U), in 20th Ann. Tri-Service Radar Symposium, p. 351.

<sup>8.</sup> Herper, J.C., Esposito, F.J., Rothenberg, C., and Hessel, A. (1977)
Surface resonances in a radome covered dipole array, 1977 International
Symposium Antennas Propag. Digest, p. 198.

# References

- 1. Herper, J.C., Hessel, A., and Tomasic, B. (1985) Element pattern of an axial dipole in a cylindrical phased array, Part 1: Theory, Part 2: Element design and experiments, IEEE Trans. Antennas Propag., AP-33.
- 2. Hessel, A. (1972) Mutual coupling effects in circular arrays on cylindrical surfaces aperture design implications and analysis, Phased Array Antennas, Artech House, Dedham, Mass., p. 273.
- 3. Jasik, H. (1959) Antenna Engineering Handbook, McGraw-Hill, New York, pp. 3-13 to 3-15.
- 4. Sureau, J.C., and Hessel, A. (1971) Element pattern for circular arrays of waveguide-fed axial slits on large conducting cylinders, IEEE Trans. Antennas Propag. AP-19: 64-76.
- 5. Sureau, J.C., and Hessel, A. (1972) Realised gain function for a cylindrical array of open-ended waveguides, Phased Array Antennas, Artech House, Dedham, Mass., p. 315.
- 6. Provencher, J.H. (1972) Conformal arrays on surfaces with rotational symmetry, Phased Array Antennas, Artech House, Dedham, Mass., p. 301.
- 7. Reale, J.D. (1974) PAR hardened cross-dipole array (U), in 20th Ann. Tri-Service Radar Symposium, p. 351.
- 8. Herper, J.C., Esposito, F.J., Rothenberg, C., and Hessel, A. (1977) Surface resonances in a radome covered dipole array, 1977 International Symposium Antennas Propag. Digest, p. 198.

# Nomenclature

```
Polar angle measured from the cylinder axis
         Circumferential angle measured from element broadside
         = (90^{\circ} - \theta) - Elevation angle measured from normal to axis
\theta_0, \phi_0 Beam pointing direction for active phased array
         Array circumference
ka
         Circumferential element spacing
р
         Axial element spacing
ď
L
         Dipole length
         Dipole spacing from cylindrical ground
8
         Dipole width
14
h
         Dipole feed gap
         Number of dipoles in each ring (192)
N
f
         Operating frequency
         Design center frequency
\mathbf{f_c}
```

NOTE: All lengths in wavelengths at the test frequency.